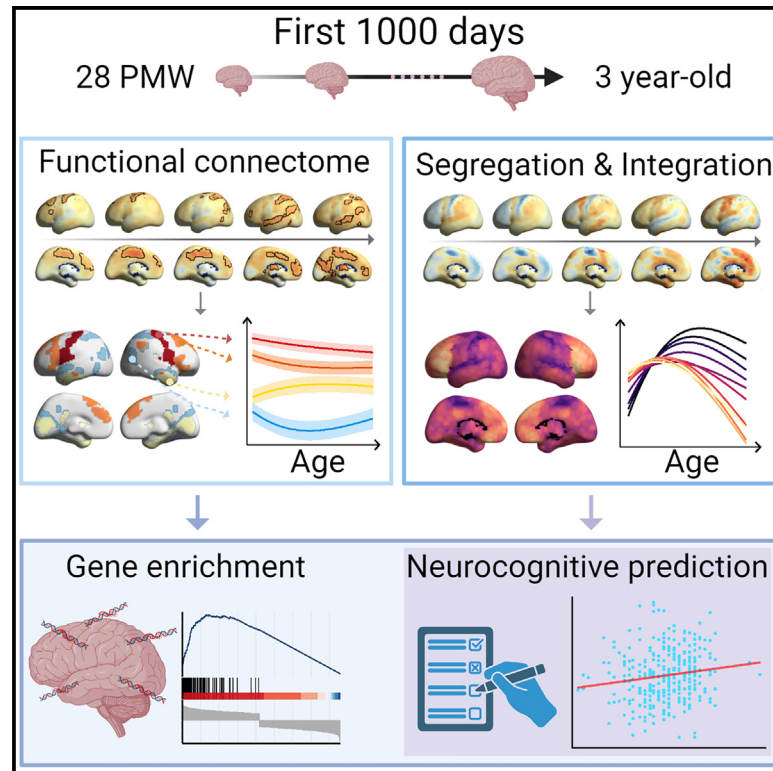


Development of segregation and integration of functional connectomes during the first 1,000 days

Graphical abstract



Authors

Qionglin Li, Mingrui Xia, Debin Zeng, ..., Ran Huo, Shuyu Li, Yong He

Correspondence

shuyuli@bnu.edu.cn (S.L.),
yong.he@bnu.edu.cn (Y.H.)

In brief

Li et al. report the maturational principles of network segregation and integration of the functional connectome during the first 1,000 days of human life. They also show the importance of early connectome remodeling for later neurocognitive outcomes and establish the associations with gene expression signatures of neurodevelopment and metabolism.

Highlights

- Brain hubs shift from primary to association regions during the first 1,000 days of life
- Functional segregation and integration develop along an anterior-posterior axis
- Neonatal connectomes predict cognitive and language outcomes at 1.5 years of age
- Network growth is regulated by genes involved in neurodevelopment and metabolism



Article

Development of segregation and integration of functional connectomes during the first 1,000 days

Qionglin Li,^{1,2,3} Mingrui Xia,^{1,2,3} Debin Zeng,⁴ Yuehua Xu,^{1,2,3} Lianglong Sun,^{1,2,3} Xinyuan Liang,^{1,2,3} Zhilei Xu,^{1,2,3} Tengda Zhao,^{1,2,3} Xuhong Liao,⁵ Huishu Yuan,⁶ Ying Liu,⁶ Ran Huo,⁶ Shuyu Li,^{1,*} and Yong He^{1,2,3,7,8,*}

¹State Key Laboratory of Cognitive Neuroscience and Learning, Beijing Normal University, Beijing 100875, China

²Beijing Key Laboratory of Brain Imaging and Connectomics, Beijing Normal University, Beijing 100875, China

³IDG/McGovern Institute for Brain Research, Beijing Normal University, Beijing 100875, China

⁴Beijing Advanced Innovation Center for Biomedical Engineering, School of Biological Science & Medical Engineering, Beihang University, Beijing 100083, China

⁵School of Systems Science, Beijing Normal University, Beijing 100875, China

⁶Department of Radiology, Peking University Third Hospital, Beijing 100191, China

⁷Chinese Institute for Brain Research, Beijing 102206, China

⁸Lead contact

*Correspondence: shuyuli@bnu.edu.cn (S.L.), yong.he@bnu.edu.cn (Y.H.)

<https://doi.org/10.1016/j.celrep.2024.114168>

SUMMARY

The first 1,000 days of human life lay the foundation for brain development and later cognitive growth. However, the developmental rules of the functional connectome during this critical period remain unclear. Using high-resolution, longitudinal, task-free functional magnetic resonance imaging data from 930 scans of 665 infants aged 28 postmenstrual weeks to 3 years, we report the early maturational process of connectome segregation and integration. We show the dominant development of local connections alongside a few global connections, the shift of brain hubs from primary regions to high-order association cortices, the developmental divergence of network segregation and integration along the anterior-posterior axis, the prediction of neurocognitive outcomes, and their associations with gene expression signatures of microstructural development and neuronal metabolic pathways. These findings advance our understanding of the principles of connectome remodeling during early life and its neurobiological underpinnings and have implications for studying typical and atypical development.

INTRODUCTION

The human brain is organized as a hierarchical modular architecture to facilitate segregated and integrated processing, which is critical for maintaining brain plasticity, flexibility, and adaptability.¹ Functional segregation and integration refer to the fundamental organizational principles by which brain regions become specialized for specific functions, and these specialized regions work together as a cohesive network to support complex cognitive processing.¹ The first 1,000 days, from conception to the first 3 postnatal years,² are critical periods during which the human brain undergoes a remarkable process of growth and reorganization.^{3,4} One of the most important aspects of this process is to unravel the developmental rules of segregation and integration of functional connectomes. Understanding how these processes mature during the perinatal and early postnatal periods is a crucial step in elucidating the mechanisms underlying typical and atypical development.

During the third trimester, the human brain undergoes a series of rapid and complex cellular and molecular processes

that significantly shape the architecture of the cerebral cortex. These processes include axonal growth,⁵ dendritic arborization,^{6,7} synapse formation,⁸ and neuronal apoptosis.⁹ After birth, neurogenesis¹⁰ and the migration of new neurons¹¹ occur during the first months of life, together with an increase in neuronal complexity¹² and synapse number.⁸ These microstructural changes during the first years of life reshape the maturation of the network architecture of structural and functional connectomes at the macroscale. In particular, several studies have documented that white matter tracts and networks are largely established at birth but that intrinsic or spontaneous functional networks continue to develop rapidly from the perinatal period through the first years of life. A sequential and hierarchical development of functional connectomes has been observed, with the primary cortex maturing first and gradually progressing to higher-order areas of the cortex.^{13–17} Specifically, in our previous work, we observed predominantly functional connectivity changes in primary brain systems and less in higher-order default mode and executive control regions, accompanied by increased functional segregation during



the third trimester.¹³ The primary sensorimotor and auditory networks resembled their adult maps, whereas the higher-order salience and frontoparietal networks were immature at the end of the first year.¹⁷ At the network level, functional hubs are mainly located in the primary visual, auditory, and sensorimotor areas around the time of birth.^{13,16} At 2 years of age, bilateral superior medial frontal regions emerge as hubs, suggesting a shift toward higher-order cognitive functions at this time, with the distribution of functional hubs at this age being significantly different from that in adults.¹⁸ The human brain already exhibits a small-world topological architecture at birth, allowing for efficient information segregation and integration with low wiring and energy costs. The efficiency of whole-brain wiring improves remarkably by 1 year of age and becomes more stable by 2 years of age.¹⁸ After 2 years of age, brain development is predominantly characterized by the reorganization, fine-tuning, and remodeling of established major circuits and networks.³ This stage involves the refinement and optimization of existing neural connections and the shaping of functional brain architecture. Previous studies have been limited in scope because they were either cross-sectional in design^{13,15,19} or focused on narrow age ranges, such as the perinatal period^{13,14,16} or the first^{17,20} or second^{18,21} years of life. These studies did not provide a continuous understanding of connectome developmental trajectories during the perinatal and postnatal periods. Thus, the continuous, longitudinal developmental process of functional segregation and integration of the whole brain connectome during the first 1,000 days remains largely unexplored. Furthermore, the potential genetic contributions underlying connectome growth during this critical period remain to be elucidated.

Gene expression plays a critical role in regulating human neurodevelopment, with spatiotemporal dynamics that vary between brain regions.²² The timing of key neurodevelopmental processes coincides with the developmental trajectories of genes involved in neuronal differentiation, synaptogenesis, and myelination.²³ During perinatal development, aerobic glycolysis (AG) is the predominant metabolic pathway to support the molecular demands of neuronal proliferation.²⁴ Later during postnatal development, AG continues to support the maturational changes of neurons, such as myelination, synaptogenesis, and axonal extension. AG produces acetyl-coenzyme A (CoA), which is essential for fatty acid synthesis required for myelination^{25,26} and amino acid synthesis required for synaptogenesis and axonal extension.²⁷ A meta-analysis of previous studies on brain glucose and oxygen metabolism shows that AG increases during childhood, coinciding with the period of highest synaptic growth rates.²⁸ Brain regions with higher levels of AG show increased gene expression related to synapse formation and growth. In our previous work, combining neuroimaging and computational models, we found significant associations between total axonal projection length and AG across brain regions, with higher levels observed primarily in the default mode and prefrontal regions.²⁹ Furthermore, the cerebral metabolic rate of glucose is related to the degree of functional connectivity, which represents the number of connections of network nodes supporting both functional integration (global degree)

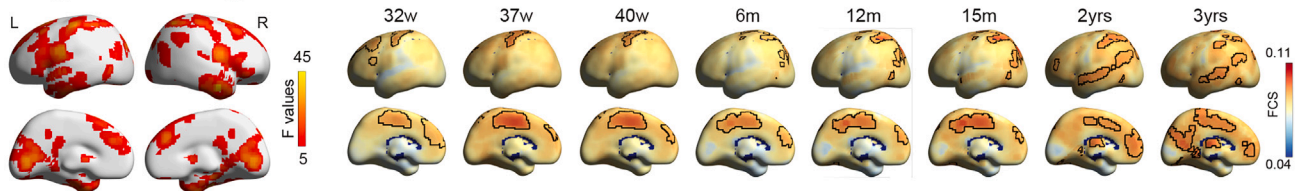
and functional segregation (local degree) in the brain.³⁰ Interestingly, these functional hub regions have a relatively high metabolic rate in infants.³¹ Therefore, we speculate that the maturation process of the connectome segregation and integration during the first 1,000 days is influenced by the expression levels of genes involved in metabolism and neurodevelopment.

To fill these critical knowledge gaps, this study investigated the continuous developmental trajectory of connectome segregation and integration during the first 1,000 days and its association with gene expression signatures. We used a large sample of high-quality longitudinal neuroimaging data, comprising 930 scans from 665 infants, obtained from the Developing Human Connectome Project (dHCP)³² and the Baby Connectome Project (BCP).³³ These infants underwent task-free functional MRI (tf-fMRI) scans at different ages, ranging from 28 postconceptional weeks to 3 postnatal years. To comprehensively map the developmental trajectory, we used a set of segregation and integration measures based on high-resolution functional connectomes. These measures allow us to capture the intricate patterns of functional segregation and integration during this period. We also used a subset of the dHCP cohort (321 term infants) to investigate whether the neonatal functional connectome could predict neurocognitive outcomes assessed at 1.5 years of age. Finally, we examined the association between the connectome growth patterns and the transcriptome using the developmental BrainSpan Atlas.^{34,35} Through these analyses, we aim to elucidate the intricate dynamics of the functional connectome during the first 1,000 days and provide insights into the potential molecular mechanisms underlying early brain development.

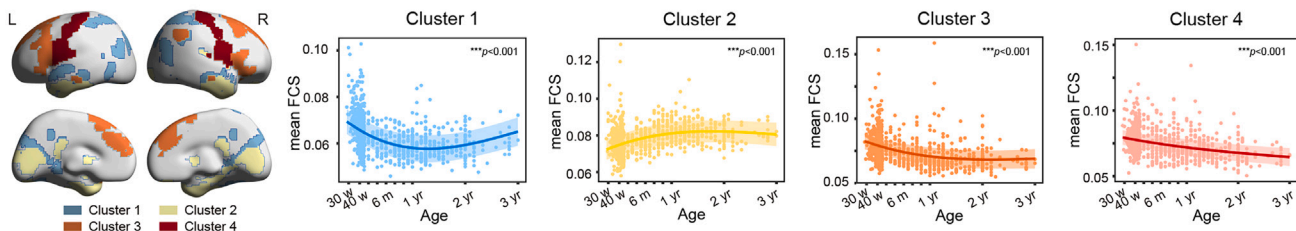
RESULTS

We conducted a comprehensive study of developmental patterns of functional connectome segregation and integration in a longitudinal sample of 665 infants aged 28 postconceptional weeks to 3 postnatal years from the dHCP and BCP projects (for the quality control process and final data distribution, see [STAR Methods](#), [Table S1](#), and [Figures S1](#) and [S2](#); for neuroimage preprocessing, see [STAR Methods](#) and [Figure S3A](#)). To capture the continuous maturational process of functional segregation and integration during the first 1,000 days, we used a generalized additive mixed model (GAMM) with age as a smooth term and subject ID as a random effect. Linear covariates such as sex, head motion within scanners, and site were included in the model. By applying the GAMM to each brain voxel, we aimed to model the non-linear growth trajectories across the cortex. Importantly, we investigated whether the developmental trajectory of functional segregation and integration exhibited spatiotemporal heterogeneity across the cortex. Using support vector regression analysis, we examined whether the neonatal functional connectome could predict neurodevelopmental outcomes at 1.5 years of age. Finally, we investigated the potential influence of differential spatiotemporal gene transcription on the development of the functional connectome. Through these analyses, we aimed to gain a comprehensive understanding of the dynamic development

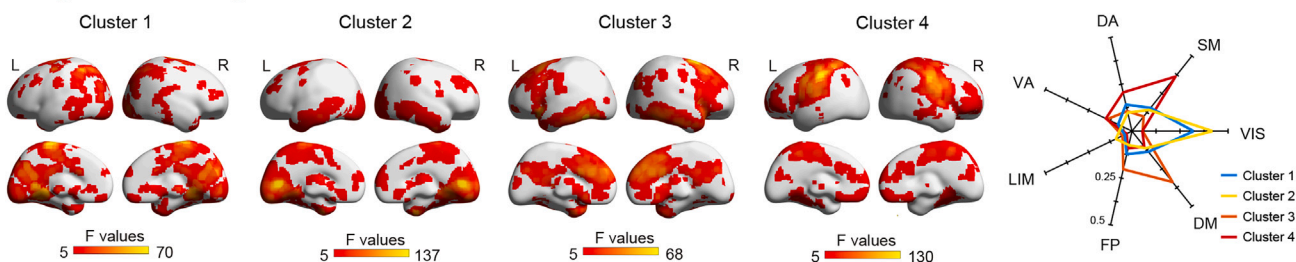
A Age-related changes in FCS



B Four clusters of significantly changed FCS



C Age-related changes of cluster-based FCS



D Hub distribution across functional systems E Age-related changes of FCS in different distance bins

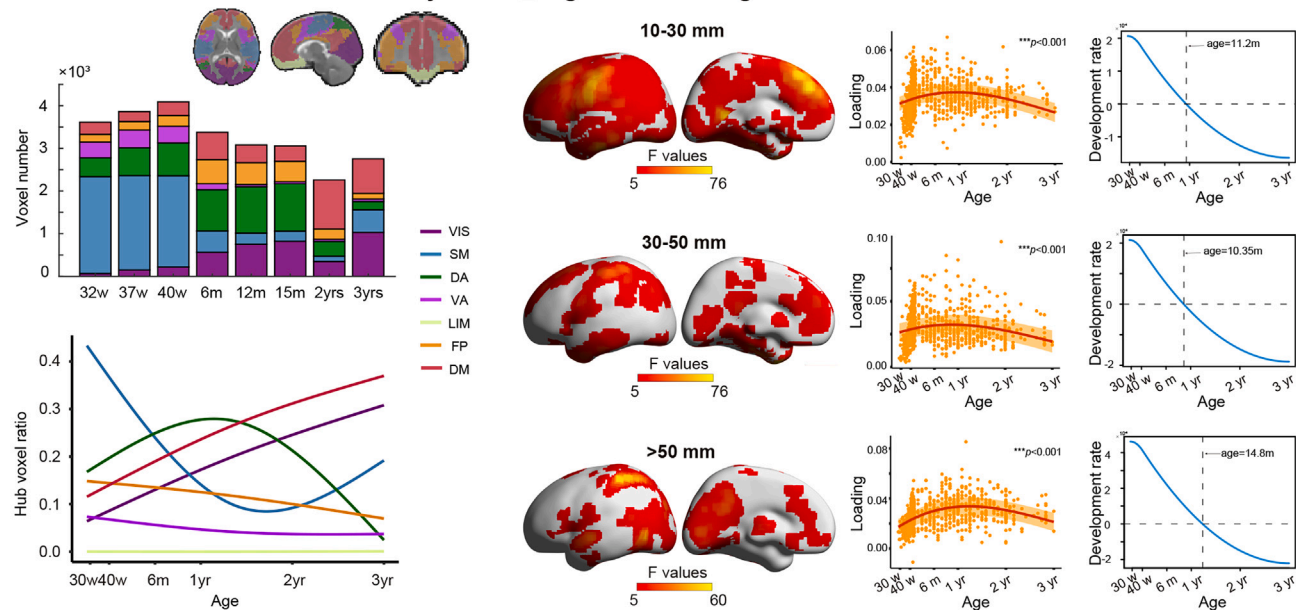


Figure 1. Development of functional connectivity

(A) Voxel-wise developmental changes of FCS. F-values obtained from the age term in GAMM were corrected using Gaussian random field method with voxel-level $p < 0.001$ and cluster-level $p < 0.05$. The fitted FCS values at different ages were mapped using the BrainNet Viewer software.³⁷ Black-outlined voxels are hubs, defined as FCS values exceeding the mean plus 1.5 times standard error.

(B) All regions with significant age-related changes in FCS were categorized into four clusters based on their similarity of developmental trajectories. For each cluster, the trajectory of the averaged FCS was delineated using different colors, with 95% confidence intervals plotted and their corresponding p values displayed.

(legend continued on next page)

of functional segregation and integration during the first 1,000 days of life.

Dominant development of local connections alongside a few global connections

Functional connectivity strength (FCS) is one of the most direct measures of overall functional connectivity (FC). Significant age-related changes in FCS during the first 1,000 days were observed primarily in the primary sensorimotor, visual, auditory, and language cortical regions as well as regions within default mode and executive control systems (Gaussian random field corrected, voxel-level $p < 0.001$, cluster-level $p < 0.05$; Figure 1A, left). The fitted FCS maps are shown on the right in Figure 1A. To illustrate the different patterns of developmental trajectories, we categorized the brain nodes with significant FCS changes into four clusters (Figure 1B, left; for details, see STAR Methods and Figure S3B). This categorization is based on the similarity of the developmental trajectories of FCS within each cluster. It is clear that different clusters show heterogeneous developmental patterns in FCS (Figure 1B, right). Specifically, cluster 1 (blue color), which is mainly located in the superior temporal, lateral occipital, and medial and lateral parietal cortices, is characterized by a U-shaped developmental curve ($F = 26.04, p < 0.001$). Cluster 2 (yellow color), which includes the medial occipital, middle, and inferior temporal cortices and the putamen, exhibits an initial increase followed by relative stability ($F = 24.61, p < 0.001$). Cluster 3 (orange color), located in the medial and lateral prefrontal cortices, shows a moderate decreasing pattern ($F = 24.61, p < 0.001$). Cluster 4 (red color), located in the sensorimotor cortex, shows an almost linear decreasing pattern ($F = 24.58, p < 0.001$). We then calculated the functional connectivity between each cluster and all voxels and found significant changes in cluster-based connectivity mainly within local functional systems (Gaussian random field corrected, voxel-level $p < 0.001$, cluster-level $p < 0.05$) (Figure 1C). The ratio of the F-values in Yeo's 7 functional systems³⁶ to the total F-value for each cluster, as shown in the radar plot, supports this finding. In addition, significant sex differences were observed in the developmental trajectories of mean FCS within cluster 1 (*Deviance* = 0.0026, $p < 0.001$). No significant sex differences were observed in the developmental trajectories within other clusters (cluster 2, *Deviance* = 0.0004; cluster 3, *Deviance* = 0.0009; cluster 4, *Deviance* = -0.0007, all $p > 0.05$), as shown in Figure S4A.

Hubs were highly connected regions, identified as FCS greater than the mean plus 1.5 times the standard deviation (Figure 1A, right). To illustrate the distribution of hubs across different functional systems, we mapped Yeo's 7 functional

systems³⁶ on the infant brain (STAR Methods). The distribution of hubs across different functional systems at different ages is shown in Figure 1D. It is clear that the distribution of hubs during the perinatal period is mainly in the sensorimotor system. In the postnatal period, hubs were predominantly found in the dorsal attention and visual systems, then transitioned to the default mode at 2 years of age, potentially undergoing reorganization by 3 years of age. The hub voxel ratio, calculated as the number of voxels in each functional system divided by the total number of hub voxels, changed significantly with age (all $p < 0.001$). In particular, the hub voxel ratio in the sensorimotor system initially decreased from a relatively high level and then increased to some extent. The hub voxel ratio of the dorsal attention system follows an increasing and then decreasing trajectory, while the default mode and visual systems continue to increase, with the default mode system having a higher ratio.

To gain a better understanding of the spatial extent of connectivity development, we examined age-related changes in FCS across distances. We found extensive development of short-range FCS throughout the brain (10–30 mm, Gaussian random field corrected, voxel-level $p < 0.001$, cluster-level $p < 0.05$) (Figure 1E). Significant medium- to long-range FCSs were observed in a few brain regions (>30 mm, Gaussian random field corrected, voxel-level $p < 0.001$, cluster-level $p < 0.05$). To further investigate the developmental trajectory of FCS across different distance bins, we performed a principal-component analysis (PCA) on FCS within each distance bin. This approach considered the developmental trajectory of the brain rather than focusing on a single voxel property. The first principal components (PCs) from each PCA explained 32%, 27%, and 18% of the variance in developmental profiles within distance bins, respectively. FCS followed an inverted U-shaped developmental curve in all distance bins (short: $F = 14.14, p < 0.001$; medium: $F = 10.49, p < 0.001$; long: $F = 29.72, p < 0.001$). The peak age of FCS differed between distance bins, with short to medium connectivities, peaking (84.8 weeks and 81.4 weeks, approximately 10–11 months) earlier than long connectivities (99.2 weeks, approximately 15 months).

In summary, significant developmental trajectories in the FCS during the first 1,000 days are mainly located in the primary sensorimotor, visual, auditory, and language cortical regions, as well as regions within the default mode and executive control systems. Hubs shift from primary to higher-order cortices during the critical period. The local short-range functional connections within systems contribute much more to these developmental changes.

(C) Cluster-based functional connectivity development. For each cluster, the functional connectivity was computed between averaged time series of the cluster and all brain voxels. F-maps are obtained from the voxel-wise GAMM of functional connectivity. The radar plot represents the ratio of the F-values in each functional system to the total F-value.

(D) Hub distribution across different functional systems. The hub voxel numbers in each system at various ages are shown in a bar plot. The age-related changes of the hub voxel ratio in each system were fitted with GAMM, respectively.

(E) Age-related changes in FCS across different distance bins. F-maps are from the voxel-wise GAMM in each distance bins (left). PCA was performed on FCS values within each bin, with the first PCA loadings representing the overall developmental trajectory of the brain (center). The curve of development rate was derived by calculating the first difference of the loading curve (right). Dotted lines indicate the ages when the development rate is zero.

FCS, functional connectivity strength; VIS, visual; SM, somatomotor; DA, dorsal attention; VA, ventral attention; LIM, limbic; FP, frontoparietal; DM, default-mode; w, postconceptional week; m, postnatal month; yr, postnatal year.

Development of functional segregation and integration diverged along an anterior-posterior axis

Previous cross-sectional studies of brain networks have suggested a gradual enhancement of functional segregation during the third trimester and early postnatal period, followed by a potentially slower growth during infancy.^{13,18} Therefore, we aimed to investigate whether the developmental trajectory of functional segregation follows a non-linear pattern, characterized by an initial increase followed by a decrease, and exhibits spatial heterogeneity across the cortex. We also aimed to uncover the developmental pattern of functional integration, which remains unknown. We used the clustering coefficient, a common measure of functional segregation, which quantifies the extent to which a node's neighbors are interconnected in the graph. Our analysis revealed that the overall mean clustering coefficient across the cortex showed significant age-related changes, following an inverted U-shaped developmental curve during the first 1,000 days ($F = 11.07, p < 0.001$) (Figure 2A). We also examined the developmental patterns of functional integration by analyzing nodal efficiency, a measure that quantifies the efficiency with which a node communicates with other nodes. As shown in Figure 2A, mean nodal efficiency showed significant changes with age, following a U-shaped developmental trajectory ($F = 5.83, p = 0.005$). As shown in Figure S4B, significant sex differences were evident in the developmental trajectories of the mean clustering coefficient (*Deviance* = 0.067, $p = 0.007$). In contrast, the developmental trajectories of mean nodal efficiency showed no significant sex differences (*Deviance* = 0.007, $p = 0.24$).

To further investigate the progression of functional segregation and integration changes across the cortex, we performed data-driven PCA on the clustering coefficient and nodal efficiency at the voxel level, respectively, as shown in Figure 2B. This approach considered the entire developmental trajectory of the graph theory measures rather than focusing on a single age-related property. The first PC from the PCA explained 27% of the variance in the developmental profiles of the clustering coefficients. Notably, this principal developmental axis (Figure 2C) closely resembled the variation in functional connectivity profiles along the anterior-posterior (A-P) axis in neonates,³⁸ which is considered an immature sensorimotor-association (S-A) axis. The developmental axis of the clustering coefficient suggests that the spatial and temporal maturation of functional segregation aligns with the A-P axis. To visually represent the developmental trajectories of the clustering coefficient along the A-P axis, we divided the axis into 10 decile bins and calculated the average clustering coefficient across all voxels within each bin. The maturational trajectories all changed significantly with age (all $p < 0.001$) and diverged continuously along the A-P axis (Figure 2C). For node efficiency, the first PC derived from the PCA explained 45% of the variance in the developmental profiles of node efficiency. Notably, the principal developmental axis for node efficiency also varied along the A-P axis. The developmental trajectories across the 10 decile bins showed a U-shaped curve (all $p < 0.001$) with continuous variation along the A-P axis (Figure 2C). This analysis revealed a continuous spectrum of developmental trajectories that mirrored the patterns observed at the voxel level.

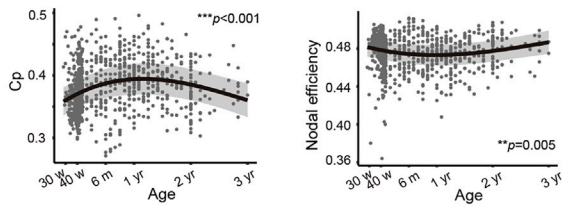
Significant age-related changes in clustering coefficient at the voxel level were mainly observed in sensorimotor, visual, superior temporal, prefrontal, dorsal attention, and subcortex regions (Gaussian random field corrected, voxel-level $p < 0.001$, cluster-level $p < 0.05$; Figure 2D). From the fitted clustering coefficient maps shown here, the overall clustering coefficient showed an increasing and decreasing trend with the highest values in the sensorimotor and visual cortex. Specifically, the clustering coefficient in the visual cortex showed an initial increase then a decrease in its developmental curve (visual: $F = 50.11, p < 0.001$), while the superior temporal and sensorimotor cortices followed first a slight increase followed by a decrease in their developmental curves (superior temporal: $F = 34.05, p < 0.001$; sensorimotor: $F = 33.83, p < 0.001$). The clustering coefficient of the medial prefrontal cortex (mPFC) and thalamus decreased with age (mPFC: $F = 25.75, p < 0.001$; thalamus: $F = 8.73, p < 0.001$). For nodal efficiency, the significantly changed regions are similar to those of the clustering coefficient (Gaussian random field corrected, voxel-level $p < 0.001$, cluster-level $p < 0.05$; Figure 2E). The fitted nodal efficiency maps showed that the overall nodal efficiency tended to decrease and then increase. In fact, the nodal efficiency in different functional systems showed a U-shaped developmental curve (visual: $F = 22.37, p < 0.001$; superior temporal: $F = 13.07, p < 0.001$; sensorimotor: $F = 28.35, p < 0.001$; lateral prefrontal cortex [LPFC]: $F = 15.09, p < 0.001$; putamen: $F = 12.72, p < 0.001$). The coordinates of the regions of interest [ROIs] can be found in Table S2.

Our results showed a non-linear pattern for both functional segregation, as measured by the clustering coefficient, and functional integration, as measured by the global efficiency, during the first 1,000 days. Functional segregation and integration followed different developmental trajectories, which were spatially heterogeneous across the cortex and aligned with the A-P axis.

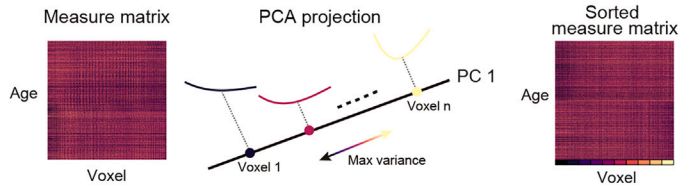
Reorganization of network modules mirrors maturation of functional segregation and integration

The development of functional systems or modules is crucial, as it underpins specialized cognitive processes and efficient information processing. To gain further insight into the developmental pattern of functional segregation and integration from a system level, we performed a modularity analysis. We used the Louvain algorithm,³⁹ a fast and accurate community detection algorithm for large networks, to explore the modular structure and examined the age-related changes in modularity (Q) and within- and between-module functional connectivity. The developmental trajectory of modularity showed an initial increase followed by a decrease ($F = 10.26, p < 0.001$; Figure 3A). Notably, the developmental trajectory of mean within-module functional connectivity closely resembled that of modularity, both of which quantized functional segregation ($F = 12.39, p = 0.001$). On the other hand, no significant change in the mean between-module functional connectivity was observed ($F = 0, p > 0.05$; Figure 3A). Besides, developmental trajectories of modularity (*Deviance* = 0.10, $p < 0.001$) and within-module functional connectivity (*Deviance* = 0.015, $p = 0.01$) revealed significant sex differences (Figure S4C). No significant sex differences were observed in the developmental trajectories of between-module

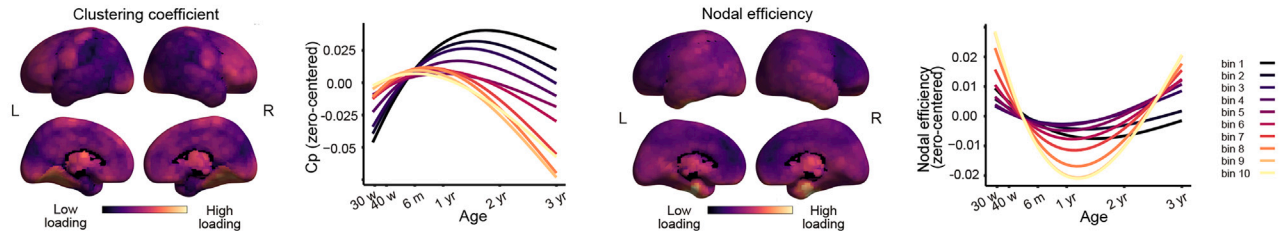
A Developmental trajectories



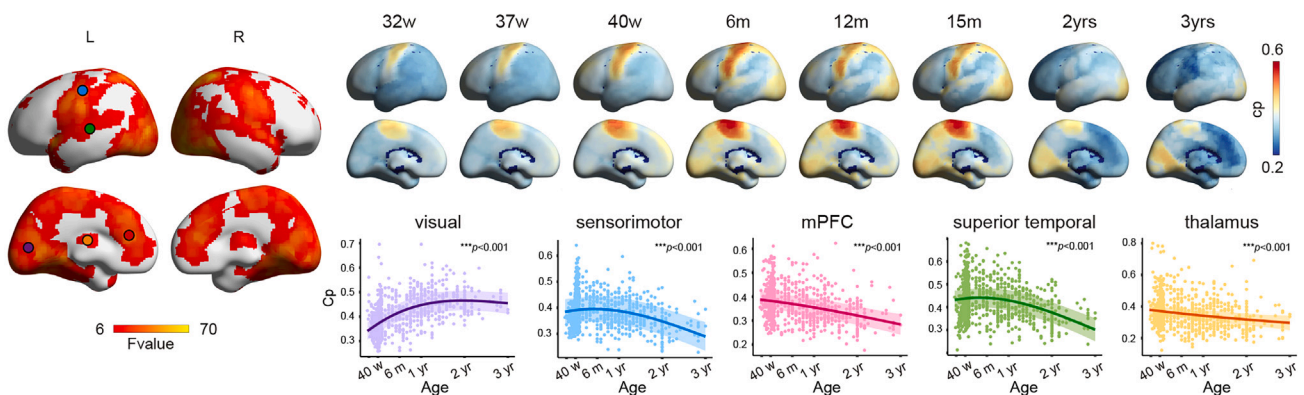
B PCA projection



C Principal developmental axis across the cortex



D Age-related changes in clustering coefficient at the voxel level



E Age-related changes in nodal efficiency at the voxel level

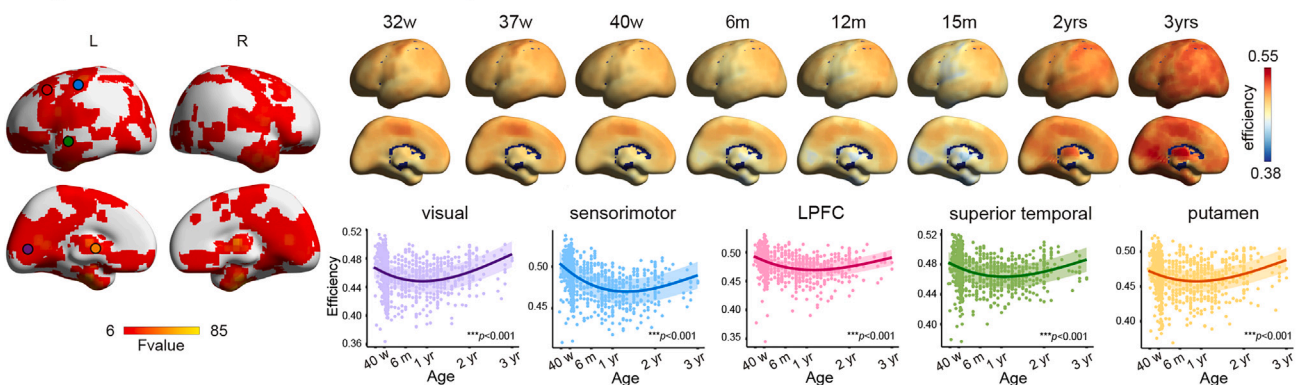


Figure 2. The developmental trajectories of functional segregation and integration exhibited spatial heterogeneity along the A-P axis of the cortex

(A) The developmental trajectories of mean clustering coefficient and nodal efficiency of all voxels with 95% confidence interval.

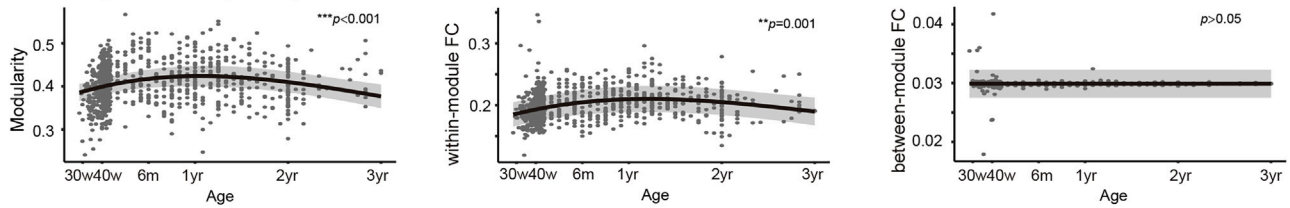
(B) Illustration of PCA on the clustering coefficient (or nodal efficiency) of all voxels.

(C) The principal developmental axis capturing cortex-wide differences in maturational patterns along the A-P direction for clustering coefficient and nodal efficiency, respectively. Maturational trajectory 10-decile bins all significantly changed with age and continuously diverged along the A-P axis.

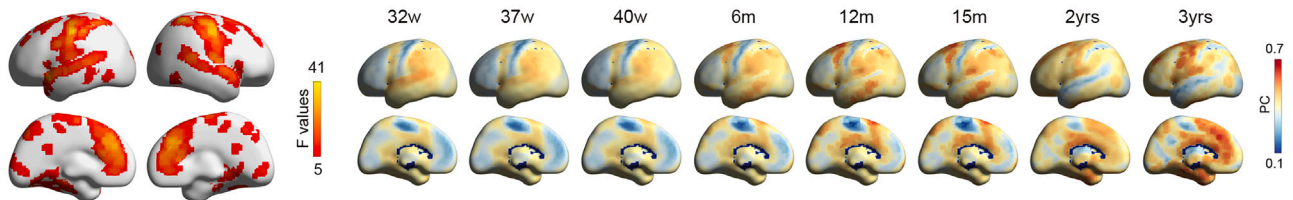
(D and E) Voxel-wise developmental changes of clustering coefficient (D) and nodal efficiency (E). F-values obtained from the age term in GAMM were corrected using the Gaussian random field method with voxel-level $p < 0.001$ and cluster-level $p < 0.05$. The fitted clustering coefficients at different ages were mapped using the BrainNet Viewer software.³⁷ The selected five seeds from the brain regions exhibited significant changes, as indicated with colored circles. Their developmental trajectories were plotted with 95% confidence interval and displayed with their corresponding p values.

Cp, clustering coefficient; mPFC, medial prefrontal cortex; LPFC, lateral prefrontal cortex; PC, principal component; w, postconceptional week; m, postnatal month; yr, postnatal year.

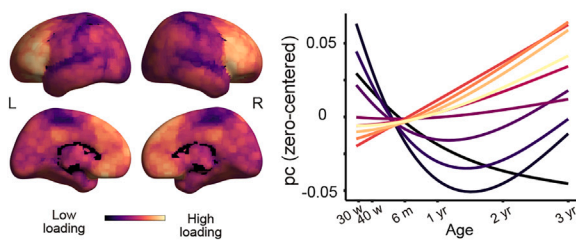
A Developmental trajectory



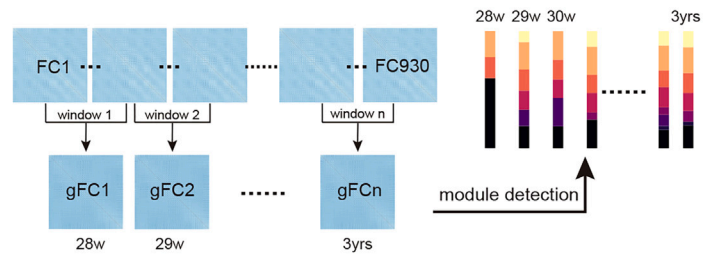
B Age-related changes of participation coefficient



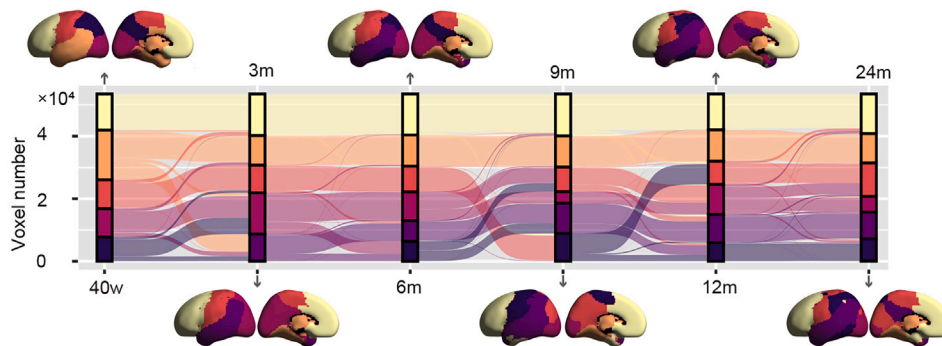
C Principal development axis across the cortex



D Module detection across age windows



E Module membership of each voxel across ages



F Flexibility map

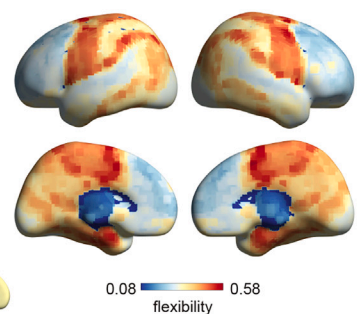


Figure 3. Reorganization of modules mirrors functional segregation and integration development

(A) Developmental trajectories of modularity, mean within-module functional connectivity, and mean between-module functional connectivity of all voxels, with 95% confidence intervals plotted and their corresponding p values displayed.

(B) Voxel-wise developmental changes of the participation coefficient. F-values obtained from the age term in GAMM were corrected using the Gaussian random field method with voxel-level $p < 0.001$ and cluster-level $p < 0.05$. The fitted participation coefficients at different ages were mapped using the BrainNet Viewer software.³⁷

(C) The principal developmental axis capturing cortex-wide differences in maturational patterns along the A-P direction for participation coefficient. Maturational trajectory 10-decile bins all significantly changed with age and continuously diverged along the A-P axis.

(D) Illustration of the process to perform module detection on the group mean functional connectivity through the sliding window method.

(E) Tracking module membership of each voxel across ages using a Sankey plot reveals a fine-grained and flexible organization of functional modules during early development.

(F) The flexibility of module assignment of each voxel was calculated as the number of times of a node changes its community assignment across age windows, normalized by the total number of possible changes.

pc, participation coefficient; FC, functional connectivity; w, postconceptional week; m, postnatal month; yr, postnatal year.

functional connectivity ($Deviance = 0.000, p > 0.05$). Furthermore, the participation coefficient, which captures the diversity of the edges of a node between modules, showed significant age-related changes in the primary sensorimotor, auditory, mPFC, and LPFC regions (Gaussian random field corrected, voxel-level $p < 0.001$, cluster-level $p < 0.05$; Figure 3B). The fitted maps of the participation coefficient at different ages showed that different regions have different developmental tendencies. Importantly, the main developmental axis for the participation coefficient was also aligned with the A-P axis. The maturation trajectories across the 10 decile bins showed a continuous spectrum of developmental patterns from an inverted U-shaped trajectory to an increasing trend (Figure 3C).

Furthermore, we examined the functional module assignment across age by performing module detection on the group functional networks obtained through the sliding window of age, as shown in Figure 3D. The module assignment of each voxel across age is shown in Figure 3E. Notably, the sensorimotor and visual cortices show changes across age with a finer subdivision, whereas the prefrontal cortex shows little change in module assignment across this period. Finally, the flexibility of module assignment was found to be greater in the sensorimotor and visual cortices compared to other regions (Figure 3F).

In summary, module-based properties reflected heterogeneity in the development of functional segregation and integration during the first 1,000 days, with within-module functional connectivity and modularity showing similar developmental patterns. The participation coefficient showed significant age-related changes along with the A-P axis. Furthermore, the increasing number of modules and highlighted regional differences, particularly in sensorimotor and visual cortices, suggested a fine-grained and flexible organization of functional modules during development.

Predicting cognitive and language development at 1.5 years from neonatal functional connectomes

We further investigated whether the development of connectome segregation and integration during early life underlies later neurocognitive growth. Using a support vector regression (SVR) model with 10-fold cross-validation, we predicted neurodevelopmental outcomes assessed at 1.5 years of age (mean age: 19.3 ± 2.22 months) from network predictors at birth (mean scan age: 41.3 ± 1.75 postconceptional weeks). All are term infants from the dHCP dataset ($n = 321$). Network predictors included mean FCS, clustering coefficient, nodal efficiency, modularity, and within-module FC. Covariates, including scan age, the interval between birth and scan, age at neurocognitive assessment, sex, and mean frame-wise displacement (mFD) were regressed out. To quantify the prediction accuracy, we calculated the Pearson correlation between the actual and predicted neurocognitive scores and assessed the significance using permutation tests ($n = 10,000$). Our analysis revealed that certain functional connectome measures at birth are predictive of later neurocognitive development. Specifically, the mean FCS ($r = 0.12, p = 0.018$), nodal efficiency ($r = 0.10, p = 0.034$), and modularity ($r = 0.10, p = 0.035$) at birth could significantly predict cognitive scores at 1.5 years of age, as shown in Figures 4A and 4B. The prediction accuracies for clus-

tering coefficient and within-module FC showed marginal significance. All measures were found to significantly predict language scores at 1.5 years of age (Figures 4A and 4C). The prediction accuracies for language scores using mean FCS, clustering coefficient, nodal efficiency, modularity, and within-module FC were $r = 0.15$ ($p = 0.004$), $r = 0.14$ ($p = 0.008$), $r = 0.11$ ($p = 0.023$), $r = 0.12$ ($p = 0.019$), and $r = 0.15$ ($p = 0.004$), respectively. However, voxel-level analyses of FCS, clustering coefficient, nodal efficiency, and participation coefficient did not yield significant predictions for neurodevelopmental outcomes. For the motor score, none of these brain measures can significantly predict the outcome.

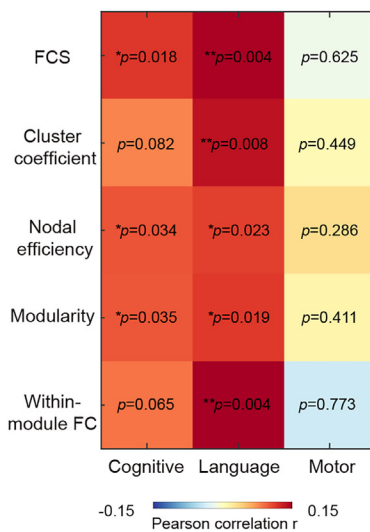
Our results highlight the potential of early postnatal network-based neuroimaging markers in predicting cognitive and language development and provide a window to explore the neural underpinnings of early development.

Distinct spatial transcriptomic pattern of functional connectivity development

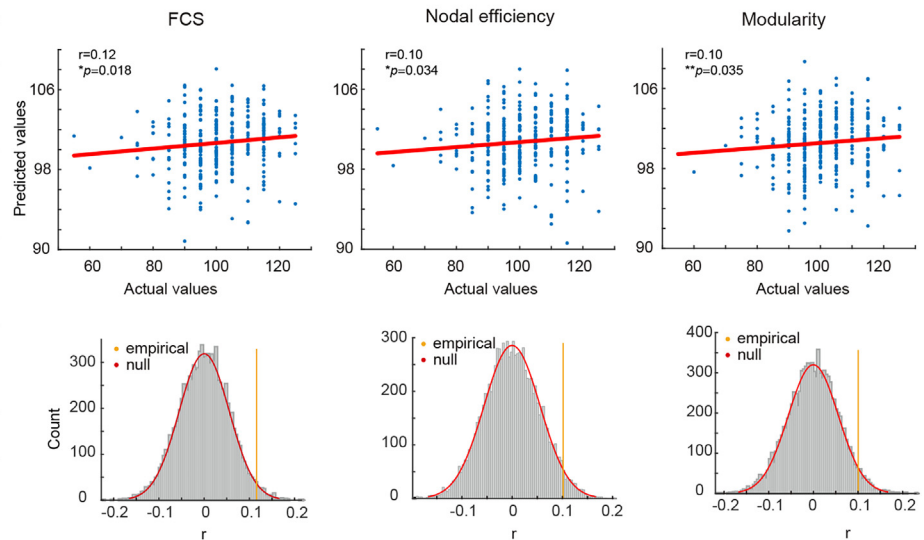
Changes in functional connectivity serve as a basis for the development of functional segregation and integration. To investigate the potential molecular mechanisms underlying functional segregation and integration, we used the developmental gene expression dataset, BrainSpan Atlas,^{34,35} to examine the gene expression differences between brain regions that showed significant and non-significant age-related FCS changes. We included the transcriptomics data of genes obtained from donors aged between 28 postmenstrual weeks and 3 years, excluding genes contributed by fewer than six donors at different ages. We included a subset of 26,874 genes (Figure 5A) derived from 105 samples, of which 61 samples were categorized as “significant (sig)” and 44 samples were categorized as “non-significant (non-sig)”. Compared to the “non-sig” regions, a total of 5,219 genes showed higher expression levels, and 5,471 genes showed lower expression levels (all $p < 0.05$, false discovery rate [FDR] corrected) in the “sig” regions. We highlighted the top 10 and bottom 10 genes with the largest absolute z values quantifying the most significant differences in the transcription levels between the “sig” and “non-sig” regions (Figure 5B). The top 10 genes are BCL11A, AC010931.2, PRKCB, NGEF, KCNH4, EPHB6, ACTN2, PEX5, TRPV6, and AC133680.1. The bottom 10 genes are ZIC1, TCF7L2, LINC00341, RP11-57H14.2, SLC6A9, SPECC1, KIF6, SYT9, CCDC48, and TPPP3.

Next, we performed Gene Ontology (GO) enrichment analysis on these genes with significant expression level differences for all the three ontology categories: biological process, molecular function, and cellular component. As shown in Figure 5C, we found that these genes were enriched in biological processes including cellular component organization or biogenesis, phosphorus metabolic process, phosphate-containing compound metabolic process, and regulation of neuron differentiation (all $p < 0.05$, FDR corrected). As for their molecular function, these genes are primarily associated with binding activities (all $p < 0.05$, FDR corrected). Moreover, they are active in cellular components related to synapses, cell projections, intracellular membrane-bound organelles, and plasma membrane-bound cell projection parts (all $p < 0.05$, FDR corrected).

A Observed r and p-values



B Prediction of cognitive scores



C Prediction of language scores

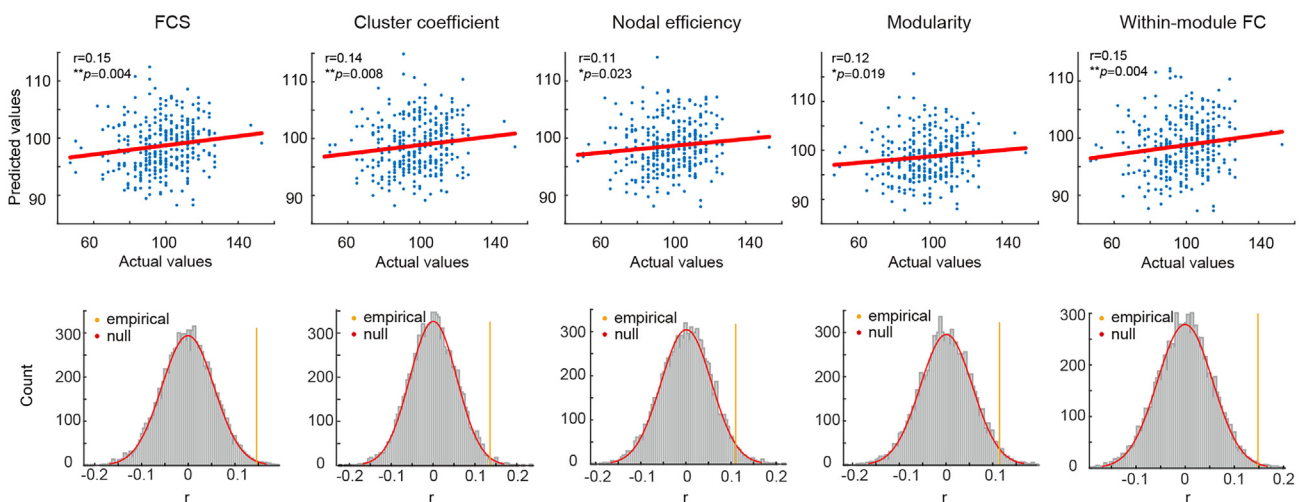


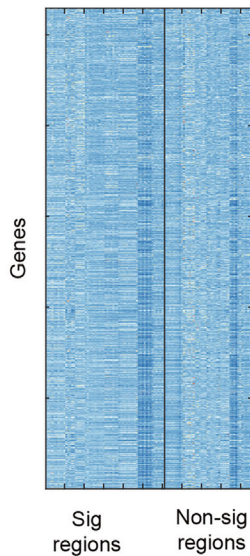
Figure 4. Predicting cognitive and language development at 1.5 years of age using neonatal functional connectomes

(A) Prediction accuracies, calculated as the Pearson correlation between the actual and predicted neurocognitive scores, and their corresponding p values were arranged in a matrix. Color intensity represents the level of prediction accuracy.
 (B) Prediction of cognitive scores at 1.5 years of age using neonatal mean FCS, nodal efficiency, and modularity, respectively.
 (C) Prediction of language scores at 1.5 years of age using neonatal mean FCS, clustering coefficient, nodal efficiency, modularity, and within-module FC, respectively. The scatterplot visualizes the correlation between the actual and predicted neurocognitive scores. The histogram displays the distribution of prediction accuracies derived from the permutation test.

We further performed gene set enrichment analysis to examine whether typical neurodevelopmental processes and key neuronal metabolic pathway-related genes were significantly enriched at the top or bottom of our ranked gene list (Figure 5B). The eight gene sets selected based on previous work covered typical neurodevelopmental processes,²² including dendrite development, synapse development, neuronal differentiation, neuronal migration, axon development and myelination, and key neuronal metabolic pathways, including AG²⁸ and oxidative phosphorylation.⁴⁰ As shown in Figure 5D, we found that the genes related to neuronal metabolic pathways

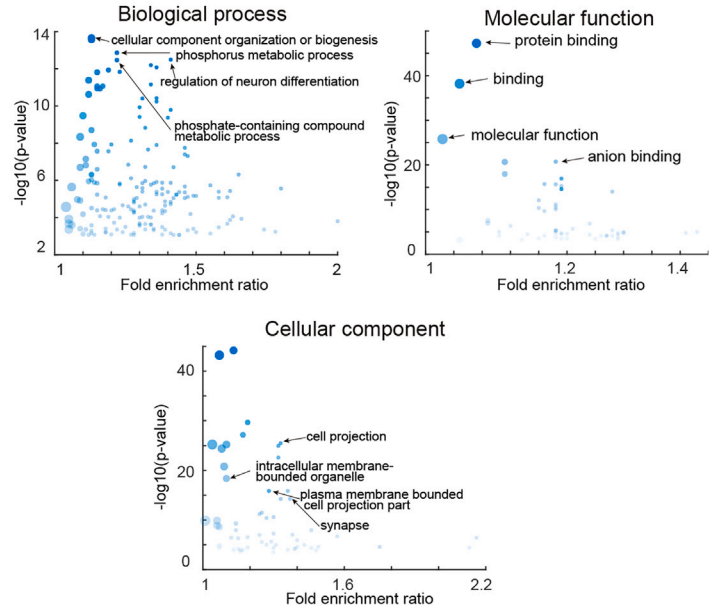
were significantly enriched at the top of our ranked gene list (AG: normalized enrichment score [NES] = 6.18, $p = 0.0003$; oxidative phosphorylation: NES = 2.13, $p = 0.0024$). The genes related to dendrite and synapse development were significantly enriched at the top of our ranked gene list (dendrite development: NES = 2.07, $p = 0.0024$; synapse development: NES = 3.31, $p = 0.0003$). The genes related to neuron differentiation and migration showed significant enrichment at the top of our ranked gene list (neuron differentiation: NES = 4.18, $p = 0.0003$; neuron migration: NES = 3.16, $p = 0.0003$). In addition, the genes related to axon development and

A Gene expression matrix B Selected genes



Gene	Z-value
BCL11A	5.26
AC010931.2	5.22
PRKCB	5.13
NGEF	5.12
KCNH4	5.09
EPHB6	5.04
ACTN2	5.02
PEX5	5.02
TRPV6	4.98
AC133680.1	4.93
.....
ZIC1	-5.48
TCF7L2	-5.50
LINC00341	-5.65
RP11-57H14.2	-5.70
SLC6A9	-5.71
SPECC1	-5.74
KIF6	-5.75
SYT9	-5.76
CCDC48	-5.80
TPPP3	-6.15

C Enriched GO terms



D Gene set enrichment analysis

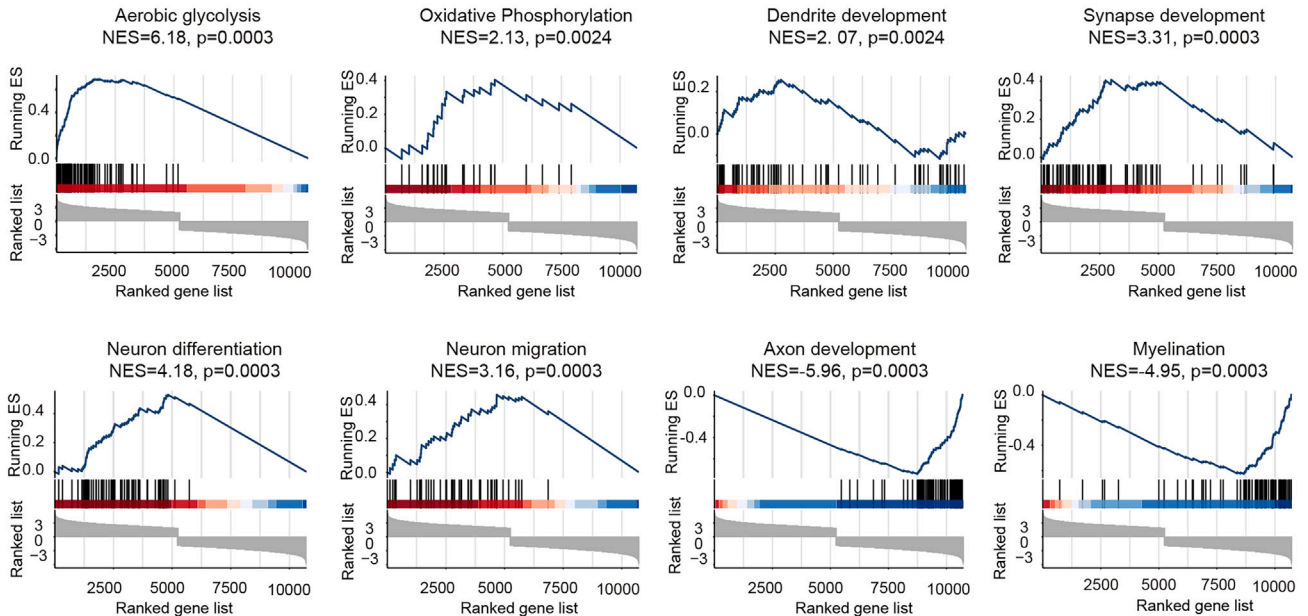


Figure 5. Distinct spatial transcriptomic pattern of FCS development

(A) The gene expression matrix of samples was assigned as the “significant (sig)” and “non-significant (non-sig)” regions.
 (B) The selected genes with significant expression differences between “sig” and “non-sig” regions. Positive z values indicate a higher transcription level in the “sig” regions than in the “non-sig” regions, while negative z values indicate a lower transcription level in the “sig” regions than the “non-sig” regions.
 (C) The Gene Ontology (GO) enrichment analysis on these genes with significant expression level differences for the three ontology categories: biological process, molecular function, and cellular component.
 (D) Gene set enrichment analysis revealed whether the genes related to typical neurodevelopmental processes and key neuronal metabolic pathways were significantly enriched at the top or bottom of our ranked gene list. The selected gene sets were involved in six typical neurodevelopmental processes (dendrite development [103 genes], synapse development [104 genes], neuron differentiation [103 genes], neuron migration [101 genes], axon development [101 genes], and myelination [105 genes]) and two main neuronal metabolic pathways (AG [116 genes] and oxidative phosphorylation [82 genes]). The normalized enrichment scores and their corresponding p values are shown on the top of the subplots.
 GO, Gene Ontology; NES, normalized enrichment score.

myelination were significantly enriched at the bottom of our ranked gene list (axon development: NES = -5.96 , $p = 0.0003$; myelination: NES = -4.95 , $p = 0.0003$). All p values were adjusted for multiple comparisons using FDR.⁴¹

DISCUSSION

The investigation of functional segregation or integration at early stages has been the subject of several studies. However, these studies have relied on small sample sizes and limited imaging data, either during the perinatal¹³ or postnatal period.^{18,20,21} Consequently, the dynamic and complex early functional brain development has not been adequately characterized. To address this gap, our study utilized two high-quality datasets with comprehensive coverage of both the perinatal (28–45 post-menstrual weeks) and postnatal (0–36 months) periods. Our analysis revealed a priority development of local segregation and hub relocation from the primary to the higher-order cortex, driven by the development of FCS within systems. We found that regional developmental trajectories of functional segregation and integration diverged in a continuous manner across the anterior-posterior axis. We also showed that early connectome growth is predictive of later cognitive and language development. The underlying mechanism driving such a developmental pattern is involved in the regulation of genes related to typical neurodevelopmental processes and metabolic pathways.

Building on our previous work focusing on the third trimester,¹³ in the present study, we observed distinct growth patterns of FCS across various regions, aligning with the timelines of synaptogenesis and synaptic pruning. For different cortical areas, synaptogenesis occurs rapidly around the time of birth but peaks at different ages.^{42,43} For example, the visual cortex experiences rapid synapse formation between 3 and 4 months and reaches maximum density between 4 and 12 months, whereas synapse density in the prefrontal cortex increases more gradually and peaks after the first year of life.⁴² After birth, a process known as pruning, which refines neural connections, becomes more active. Pruning is particularly pronounced in sensory and motor cortices immediately after birth, followed by association cortices.⁴⁴ Positron emission tomography (PET) imaging supports these findings, as glucose uptake rates in different brain regions change with age, with the sensorimotor cortex activity being highest in newborns and significant increases observed in the occipital cortices by 3 months of age.⁴⁵ The molecular mechanisms driving these developmental patterns involve genes critical for synapse formation and neuronal activity, such as SYT9 and EphB6. SYT9 plays a vital role in synaptic transmission and neuronal communication,⁴⁶ which is essential for the rapid network formation in the early stages. EphB6, a member of the ephrin receptor family, promotes cell adhesion and migration,⁴⁷ a process that is thought to be essential for the formation and maintenance of neural circuits. These imaging-based findings align with the developmental trajectory predicted by changes in synaptic density and activity and provide a window into the dynamic processes that shape early brain development.

The development of functional connectivity within specific systems largely accounts for the observed changes in FCS.

Fair et al. suggested that the most efficient way for children to respond to processing demands is to use more “local” level interactions as compared to adults.⁴⁸ When performing identical tasks on lexical processing tests, a large number of visual regions are activated in children, but strong visual activation is much more restricted in adults.⁴⁹ In particular, we found that the distribution of hubs shifted from primary regions to higher-order cortices. Hubs are predominantly found in the primary areas, which are critical for early survival during the perinatal period. However, during the transition from the perinatal to the postnatal period, the primary sensorimotor cortex experiences a decrease in FCS, causing it to relinquish its hub position. By 2 years of age, the default mode system, which is spatially distributed across the cortex, emerges as hubs, replacing the dorsal attention and visual cortices. Our results highlight that the brain’s functional network is reorganized from a local proximity-based pattern to a more functional distribution pattern during the first 1,000 days.

Human brain networks show dominant short-range connections alongside a few long-range connections, predominantly linked to hub regions, governed by a trade-off between minimizing cost and maximizing topological efficiency. An increase of short- to medium-distance connections was found before the age of 1 year, which may largely benefit the specialization of local communities. Thereafter, a decrease in both short- to medium-range connections and the local clustering coefficient may reflect rapid increases of synaptic density after birth, peaking at 1–2 years of age and decreasing in later childhood.⁵⁰ Long-range connections, which are primarily involved in global information integration, developed later in the early postnatal period, suggesting the development of local segregation followed by global integration at this time. The delay in the emergence of long-range connections compared to short- to medium-range connections could be due to the completion of connection formation in existing neurons, where axonal growth cones have to travel longer distances to find unoccupied space on target neurons.⁵¹ Previous studies have shown that cerebral blood flow, which is an adequate surrogate for cerebral metabolism, correlated more strongly with long-range FCS than short-range FCS,⁵² suggesting that long-range connections are more closely to blood/energy supplies to facilitate their greater involvement in neural processes.⁵³ We conclude that the early developmental mechanism of the human brain appears to prioritize the local connectivity of brain regions necessary for survival by allocating limited energy.

The developmental trajectories of both segregation and integration measures showed spatial heterogeneity along the A-P axis of the cortex, which is considered to be an immature S-A axis.³⁸ From infancy to adulthood, functional segregation and integration mature along the S-A axis.⁵⁴ Our results fill existing gaps by revealing the developmental pattern of functional segregation and integration during the first 1,000 days of life. Cortical patterning is influenced by thalamocortical inputs and transcription factors expressed along the anterior-medial to posterior-lateral axis.⁵⁵ Alignment of developmental programs with the neuroaxis is a fundamental aspect of early cortical development. The spatial and temporal regulation of developmental programs during embryonic and early postnatal development is

governed by major organizational axes. Neurobiological events may contribute to the underlying mechanisms. Spatiotemporal gradients between and within brain subdivisions occur in almost all aspects of neural development, including neurogenesis, maturation of cellular processes, synaptogenesis, and myelination.^{56–58} Postmortem and anatomical MRI studies show that myelination progresses in an A-P direction, following the general pattern of maturation of neural circuits.^{59–61} There is also an A-P gradient in the timing of neurogenesis across the cortex.⁶² Changes in metabolic activity, as observed by PET imaging, show spatial and temporal patterns similar to myelination and neurogenesis.⁶³

During the third trimester, the brain undergoes significant development, including rapid neuronal growth, synaptogenesis, and the beginning of functional network formation.³ This period sets the stage for the sensory and cognitive abilities that will continue to develop after birth. The transition from birth to early childhood represents a significant phase of adaptability and plasticity in the brain, with the neonatal period acting as a critical point that strongly influences the direction and pace of postnatal neurodevelopment. The cognitive prediction findings in this study highlight that the functional connectome patterns established at birth are key indicators of cognitive and language outcomes in early childhood, consistent with previous studies.^{64–66} These patterns are dynamic, shaped by prenatal development and modulated by postnatal experiences and environmental exposures. The influences of experience and environment could partly explain why the associations between imaging markers and outcomes are moderate. Functional segregation and integration are key processes that allow the brain to organize its networks for efficient information processing and integration. The balance between segregation, in which brain areas are localized to perform specialized tasks, and integration, in which different regions work together to form a unified network, is vital for sophisticated cognitive functions. Initially, the brain prioritizes functional segregation to establish specialized centers for critical tasks, such as language comprehension and sensory input. Over the first 1,000 days, the brain's functional network shifts from a pattern based on local proximity to a more distributed pattern, highlighting that the timing of connectome development is crucial for the growth and emergence of cognitive abilities.

Limitations of the study

Several limitations need to be addressed. First, to examine the developmental patterns of the functional connectome at the systems level, we adapted the adult-specific Yeo's 7 network atlas to the 6-month-old infant brain using a non-linear registration. This approach neglects the inability of the adult-based atlas to capture the extensive structural and functional changes that occur during early life. In the future, it will be important to characterize system-level development by developing fine-grained, age-progressive functional brain atlases during the first 1,000 days. Second, previous studies have shown the effects of preterm birth on brain development and later cognitive growth.^{67–69} The inclusion of data from preterm infants in our study was a pragmatic decision, motivated by the significant challenges associated with the acquisition and processing of *in utero* imaging data during the critical third trimester. Although

this inclusion provides the closest practical approximation, it complicates the interpretation of typical brain development. Third, the dHCP and BCP datasets are among the most extensive collections of neuroimaging data available, primarily consisting of samples from European and American populations. Thus, the generalizability of our study to the broader population needs to be further validated by including more participants from a wider range of ethnic and cultural contexts. Fourth, the accelerated longitudinal design of the BCP and dHCP datasets cannot fully account for individual differences. A previous study suggested that cross-sectional data may not capture the nuanced developmental changes as accurately as a purely longitudinal dataset.⁷⁰ Recognizing this limitation, we emphasize the critical need for purely longitudinal data, with initiatives such as the forthcoming Healthy Brain and Child Development (HBCD) initiative being crucial for a deeper understanding of brain developmental trajectories.

STAR★METHODS

Detailed methods are provided in the online version of this paper and include the following:

- KEY RESOURCES TABLE
- RESOURCE AVAILABILITY
 - Lead contact
 - Materials availability
 - Data and code availability
- EXPERIMENTAL MODEL AND STUDY PARTICIPANT DETAILS
 - Participants
 - Neurocognitive assessments
 - MRI quality control procedure
 - BCP task-free functional MRI quality control
- METHOD DETAILS
 - Image acquisition
 - MRI preprocessing
 - Functional connectivity matrix construction
 - Functional connectivity strength analysis
 - Graph theory measures analysis
 - Module analysis
 - Prediction analysis of neurocognitive outcomes
 - Gene expression analysis
- QUANTIFICATION AND STATISTICAL ANALYSIS
 - Developmental effects analysis

SUPPLEMENTAL INFORMATION

Supplemental information can be found online at <https://doi.org/10.1016/j.celrep.2024.114168>.

ACKNOWLEDGMENTS

This work was supported by the National Natural Science Foundation of China (82202245, 31830034, 82021004, 81972160, 32271146, and 82102131), the Startup Funds for Top-notch Talents at Beijing Normal University, and a Changjiang Scholar Professorship Award (T2015027).

AUTHOR CONTRIBUTIONS

Conceptualization, Q.L., Y.H., M.X., and S.L.; data curation, Q.L., Y.X., H.Y., Y.L., and R.H.; formal analysis, Q.L. and M.X.; investigation, Q.L., D.Z., and L.S.; funding acquisition, Q.L., Y.H., and S.L.; project administration, Y.H. and S.L.; resources, Y.H. and S.L.; software, X. Liang and Z.X.; methodology,

M.X., T.Z., and X. Liao; supervision, Y.H. and S.L.; visualization, L.S.; writing – original draft, Q.L., Y.H., and S.L.; writing – review & editing, Y.H. and S.L.

DECLARATION OF INTERESTS

The authors declare no competing interests.

Received: November 28, 2023

Revised: February 26, 2024

Accepted: April 15, 2024

REFERENCES

- Park, H.-J., and Friston, K. (2013). Structural and Functional Brain Networks: From Connections to Cognition. *Science* 342, 1238411. <https://doi.org/10.1126/science.1238411>.
- Cusick, S.E., and Georgieff, M.K. (2016). The role of nutrition in brain development: the golden opportunity of the “first 1000 days.” *J. Pediatr.* 175, 16–21.
- Gilmore, J.H., Knickmeyer, R.C., and Gao, W. (2018). Imaging structural and functional brain development in early childhood. *Nat. Rev. Neurosci.* 19, 123–137. <https://doi.org/10.1038/nrn.2018.1>.
- Cao, M., Huang, H., and He, Y. (2017). Developmental Connectomics from Infancy through Early Childhood. *Trends Neurosci.* 40, 494–506. <https://doi.org/10.1016/j.tins.2017.06.003>.
- Kostović, I., and Jovanov-Milošević, N. (2006). The Development of Cerebral Connections during the First 20–45 Weeks’ Gestation. In *Seminars in Fetal and Neonatal Medicine* (Elsevier), pp. 415–422.
- Sidman, R.L., and Rakic, P. (1973). Neuronal migration, with special reference to developing human brain: a review. *Brain Res.* 62, 1–35.
- Bystron, I., Blakemore, C., and Rakic, P. (2008). Development of the human cerebral cortex: Boulder Committee revisited. *Nat. Rev. Neurosci.* 9, 110–122. <https://doi.org/10.1038/nrn2252>.
- Huttenlocher, P.R., and Dabholkar, A.S. (1997). Regional differences in synaptogenesis in human cerebral cortex. *J. Comp. Neurol.* 387, 167–178.
- Chan, W.Y., and Yew, D.T. (1998). Apoptosis and Bcl-2 oncoprotein expression in the human fetal central nervous system. *Anat. Rec.* 252, 165–175.
- Sanai, N., Nguyen, T., Ihrie, R.A., Mirzadeh, Z., Tsai, H.-H., Wong, M., Gupta, N., Berger, M.S., Huang, E., Garcia-Verdugo, J.-M., et al. (2011). Corridors of migrating neurons in the human brain and their decline during infancy. *Nature* 478, 382–386.
- Paredes, M.F., James, D., Gil-Perotin, S., Kim, H., Cotter, J.A., Ng, C., Sandoval, K., Rowitch, D.H., Xu, D., McQuillen, P.S., et al. (2016). Extensive migration of young neurons into the infant human frontal lobe. *Science* 354, aaf7073.
- Conel, J.L.R. (1939). The postnatal development of the human cerebral cortex. *The cortex of the newborn* 1.
- Cao, M., He, Y., Dai, Z., Liao, X., Jeon, T., Ouyang, M., Chalak, L., Bi, Y., Rollins, N., Dong, Q., and Huang, H. (2017). Early Development of Functional Network Segregation Revealed by Connectomic Analysis of the Preterm Human Brain. *Cereb. Cortex* 27, 1949–1963. <https://doi.org/10.1093/cercor/bhw038>.
- Fransson, P., Skiöld, B., Horsch, S., Nordell, A., Blennow, M., Lagercrantz, H., and Åden, U. (2007). Resting-state networks in the infant brain. *Proc. Natl. Acad. Sci.* 104, 15531–15536. <https://doi.org/10.1073/pnas.0704380104>.
- Doria, V., Beckmann, C.F., Arichi, T., Merchant, N., Groppo, M., Turkheimer, F.E., Counsell, S.J., Murgasova, M., Aljabar, P., Nunes, R.G., et al. (2010). Emergence of resting state networks in the preterm human brain. *Proc. Natl. Acad. Sci.* 107, 20015–20020.
- Fransson, P., Åden, U., Blennow, M., and Lagercrantz, H. (2011). The functional architecture of the infant brain as revealed by resting-state fMRI. *Cereb. Cortex* 21, 145–154.
- Gao, W., Alcauter, S., Elton, A., Hernandez-Castillo, C.R., Smith, J.K., Ramirez, J., and Lin, W. (2015). Functional Network Development During the First Year: Relative Sequence and Socioeconomic Correlations. *Cereb. Cortex* 25, 2919–2928. <https://doi.org/10.1093/cercor/bhu088>.
- Gao, W., Gilmore, J.H., Giovanello, K.S., Smith, J.K., Shen, D., Zhu, H., and Lin, W. (2011). Temporal and Spatial Evolution of Brain Network Topology during the First Two Years of Life. *PLoS One* 6, e25278. <https://doi.org/10.1371/journal.pone.0025278>.
- Gao, W., Zhu, H., Giovanello, K.S., Smith, J.K., Shen, D., Gilmore, J.H., and Lin, W. (2009). Evidence on the emergence of the brain’s default network from 2-week-old to 2-year-old healthy pediatric subjects. *Proc. Natl. Acad. Sci. USA* 106, 6790–6795.
- Wen, X., Zhang, H., Li, G., Liu, M., Yin, W., Lin, W., Zhang, J., and Shen, D. (2019). First-year development of modules and hubs in infant brain functional networks. *Neuroimage* 185, 222–235. <https://doi.org/10.1016/j.neuroimage.2018.10.019>.
- Yin, W., Chen, M.-H., Hung, S.-C., Baluyot, K.R., Li, T., and Lin, W. (2019). Brain functional development separates into three distinct time periods in the first two years of life. *Neuroimage* 189, 715–726. <https://doi.org/10.1016/j.neuroimage.2019.01.025>.
- Kang, H.J., Kawasawa, Y.I., Cheng, F., Zhu, Y., Xu, X., Li, M., Sousa, A.M.M., Pletikos, M., Meyer, K.A., Sedmak, G., et al. (2011). Spatio-temporal transcriptome of the human brain. *Nature* 478, 483–489. <https://doi.org/10.1038/nature10523>.
- Zhu, Y., Sousa, A.M.M., Gao, T., Skarica, M., Li, M., Santpere, G., Esteller-Cucala, P., Juan, D., Ferrández-Peral, L., Gulden, F.O., et al. (2018). Spatiotemporal transcriptomic divergence across human and macaque brain development. *Science* 362, eaat8077. <https://doi.org/10.1126/science.aat8077>.
- Bauernfeind, A.L., Barks, S.K., Duka, T., Grossman, L.I., Hof, P.R., and Sherwood, C.C. (2014). Aerobic glycolysis in the primate brain: reconsidering the implications for growth and maintenance. *Brain Struct. Funct.* 219, 1149–1167. <https://doi.org/10.1007/s00429-013-0662-z>.
- Brown, A.M., Wender, R., and Ransom, B.R. (2001). Metabolic substrates other than glucose support axon function in central white matter. *J. Neurosci. Res.* 66, 839–843.
- Tekkök, S.B., Brown, A.M., Westenberg, R., Pellerin, L., and Ransom, B.R. (2005). Transfer of glycogen-derived lactate from astrocytes to axons via specific monocarboxylate transporters supports mouse optic nerve activity. *J. Neurosci. Res.* 81, 644–652.
- Goldberg, J.L. (2003). How does an axon grow? *Genes Dev.* 17, 941–958. <https://doi.org/10.1101/gad.1062303>.
- Goyal, M.S., Hawrylycz, M., Miller, J.A., Snyder, A.Z., and Raichle, M.E. (2014). Aerobic Glycolysis in the Human Brain Is Associated with Developmental and Neotenic Gene Expression. *Cell Metab.* 19, 49–57. <https://doi.org/10.1016/j.cmet.2013.11.020>.
- Chen, Y., Lin, Q., Liao, X., Zhou, C., and He, Y. (2021). Association of aerobic glycolysis with the structural connectome reveals a benefit-risk balancing mechanism in the human brain. *Proc. Natl. Acad. Sci.* 118, e2013232118.
- Tomasi, D., Wang, G.-J., and Volkow, N.D. (2013). Energetic cost of brain functional connectivity. *Proc. Natl. Acad. Sci.* 110, 13642–13647. <https://doi.org/10.1073/pnas.1303346110>.
- Chugani, H.T. (1998). A Critical Period of Brain Development: Studies of Cerebral Glucose Utilization with PET. *Prev. Med.* 27, 184–188. <https://doi.org/10.1006/pmed.1998.0274>.
- Edwards, A.D., Rueckert, D., Smith, S.M., Abo Seada, S., Alansary, A., Almalbis, J., Allsop, J., Andersson, J., Arichi, T., Arulkumaran, S., et al. (2022). The Developing Human Connectome Project Neonatal Data Release. *Front. Neurosci.* 16, 886772.

33. Howell, B.R., Styner, M.A., Gao, W., Yap, P.-T., Wang, L., Baluyot, K., Yacoub, E., Chen, G., Potts, T., Salzwedel, A., et al. (2019). The UNC/UMN Baby Connectome Project (BCP): An overview of the study design and protocol development. *Neuroimage* *185*, 891–905. <https://doi.org/10.1016/j.neuroimage.2018.03.049>.
34. Miller, J.A., Ding, S.-L., Sunkin, S.M., Smith, K.A., Ng, L., Szafer, A., Ebert, A., Riley, Z.L., Royall, J.J., Aiona, K., et al. (2014). Transcriptional landscape of the prenatal human brain. *Nature* *508*, 199–206. <https://doi.org/10.1038/nature13185>.
35. Li, M., Santpere, G., Imamura Kawasawa, Y., Evgrafov, O.V., Gulden, F.O., Pochareddy, S., Sunkin, S.M., Li, Z., Shin, Y., Zhu, Y., et al. (2018). Integrative functional genomic analysis of human brain development and neuropsychiatric risks. *Science* *362*, eaat7615. <https://doi.org/10.1126/science.aat7615>.
36. Yeo, B.T., Krienen, F.M., Sepulcre, J., Sabuncu, M.R., Lashkari, D., Hollinshead, M., Roffman, J.L., Smoller, J.W., Zöllei, L., and Polimeni, J.R. (2011). The organization of the human cerebral cortex estimated by intrinsic functional connectivity. *Journal of neurophysiology* *106*, 1125–1165.
37. Xia, M., Wang, J., and He, Y. (2013). BrainNet Viewer: A Network Visualization Tool for Human Brain Connectomics. *PLoS One* *8*, e68910. <https://doi.org/10.1371/journal.pone.0068910>.
38. Larivière, S., Vos de Wael, R., Hong, S.-J., Paquola, C., Tavakol, S., Lowe, A.J., Schrader, D.V., and Bernhardt, B.C. (2020). Multiscale Structure–Function Gradients in the Neonatal Connectome. *Cereb. Cortex* *30*, 47–58. <https://doi.org/10.1093/cercor/bhz069>.
39. Blondel, V.D., Guillaume, J.-L., Lambiotte, R., and Lefebvre, E. (2008). Fast unfolding of communities in large networks. *J. Stat. Mech.* *2008*, P10008.
40. Arroyo, J.D., Jourdain, A.A., Calvo, S.E., Ballarano, C.A., Doench, J.G., Root, D.E., and Mootha, V.K. (2016). A Genome-wide CRISPR Death Screen Identifies Genes Essential for Oxidative Phosphorylation. *Cell Metab.* *24*, 875–885. <https://doi.org/10.1016/j.cmet.2016.08.017>.
41. Benjamini, Y., and Hochberg, Y. (1995). Controlling the false discovery rate: a practical and powerful approach to multiple testing. *J. Roy. Stat. Soc. B* *57*, 289–300.
42. Krasnegor, N.A., Lyon, G., and Goldman-Rakic, P.S. (1997). *Development of the Prefrontal Cortex: Evolution, Neurobiology, and Behavior* (Paul H Brookes Publishing).
43. Nelson, C.A., and Luciana, M. (2008). *Handbook of Developmental Cognitive Neuroscience* (MIT press).
44. Levitt, P. (2003). Structural and functional maturation of the developing primate brain. *J. Pediatr.* *143*, 35–45.
45. Chugani, H.T., Phelps, M.E., and Mazziotta, J.C. (1987). Positron emission tomography study of human brain functional development. *Ann. Neurol.* *22*, 487–497.
46. Haberman, Y., Grimberg, E., Fukuda, M., and Sagi-Eisenberg, R. (2003). Synaptotagmin IX, a possible linker between the perinuclear endocytic recycling compartment and the microtubules. *J. Cell Sci.* *116*, 4307–4318.
47. Matsuoka, H., Obama, H., Kelly, M.L., Matsui, T., and Nakamoto, M. (2005). Biphasic functions of the kinase-defective Ephb6 receptor in cell adhesion and migration. *J. Biol. Chem.* *280*, 29355–29363.
48. Fair, D.A., Cohen, A.L., Power, J.D., Dosenbach, N.U.F., Church, J.A., Miezin, F.M., Schlaggar, B.L., and Petersen, S.E. (2009). Functional Brain Networks Develop from a “Local to Distributed” Organization. *PLoS Comput. Biol.* *5*, e1000381. <https://doi.org/10.1371/journal.pcbi.1000381>.
49. Brown, T.T., Lugar, H.M., Coalson, R.S., Miezin, F.M., Petersen, S.E., and Schlaggar, B.L. (2005). Developmental changes in human cerebral functional organization for word generation. *Cereb. Cortex* *15*, 275–290.
50. Peter, R.H. (1979). Synaptic density in human frontal cortex — Developmental changes and effects of aging. *Brain Res.* *163*, 195–205. [https://doi.org/10.1016/0006-8993\(79\)90349-4](https://doi.org/10.1016/0006-8993(79)90349-4).
51. Kaiser, M. (2017). Mechanisms of Connectome Development. *Trends Cogn. Sci.* *21*, 703–717. <https://doi.org/10.1016/j.tics.2017.05.010>.
52. Liang, X., Zou, Q., He, Y., and Yang, Y. (2013). Coupling of functional connectivity and regional cerebral blood flow reveals a physiological basis for network hubs of the human brain. *Proc. Natl. Acad. Sci.* *110*, 1929–1934. <https://doi.org/10.1073/pnas.1214900110>.
53. Bullmore, E., and Sporns, O. (2012). The economy of brain network organization. *Nat. Rev. Neurosci.* *13*, 336–349. <https://doi.org/10.1038/nrn3214>.
54. Keller, A.S., Sydnor, V.J., Pines, A., Fair, D.A., Bassett, D.S., and Satterthwaite, T.D. (2023). Hierarchical functional system development supports executive function. *Trends Cogn. Sci.* *27*, 160–174. <https://doi.org/10.1016/j.tics.2022.11.005>.
55. O’Leary, D.D.M., Chou, S.-J., and Sahara, S. (2007). Area Patterning of the Mammalian Cortex. *Neuron* *56*, 252–269. <https://doi.org/10.1016/j.neuron.2007.10.010>.
56. Cooper, M.L., and Rakic, P. (1983). Gradients of cellular maturation and synaptogenesis in the superior colliculus of the fetal rhesus monkey. *J. Comp. Neurol.* *215*, 165–186.
57. McSherry, G.M., and Smart, I.H. (1986). Cell production gradients in the developing ferret isocortex. *J. Anat.* *144*, 1–14.
58. Rapoport, D.H., Rakic, P., and LaVail, M.M. (1996). Spatiotemporal gradients of cell genesis in the primate retina. *Perspect. Dev. Neurobiol.* *3*, 147–159.
59. Brody, B.A., Kinney, H.C., Kloman, A.S., and Gilles, F.H. (1987). Sequence of central nervous system myelination in human infancy. I. An autopsy study of myelination. *J. Neuropathol. Exp. Neurol.* *46*, 283–301.
60. Girard, N., Raybaud, C., and Du Lac, P. (1991). MRI study of brain myelination. *Journal of Neuroradiology= Journal de Neuroradiologie* *18*, 291–307.
61. Kinney, H.C., Brody, B.A., Kloman, A.S., and Gilles, F.H. (1988). Sequence of central nervous system myelination in human infancy: II. Patterns of myelination in autopsied infants. *J. Neuropathol. Exp. Neurol.* *47*, 217–234.
62. Charvet, C.J., and Finlay, B.L. (2014). Evo-devo and the primate isocortex: the central organizing role of intrinsic gradients of neurogenesis. *Brain Behav. Evol.* *84*, 81–92.
63. Tau, G.Z., and Peterson, B.S. (2010). Normal Development of Brain Circuits. *Neuropsychopharmacology* *35*, 147–168. <https://doi.org/10.1038/npp.2009.115>.
64. Xia, Y., Zhao, J., Xu, Y., Duan, D., Xia, M., Jeon, T., Ouyang, M., Chalak, L., Rollins, N., and Huang, H. (2024). Development of sensorimotor-visual connectome gradient at birth predicts neurocognitive outcomes at 2 years of age. *iScience* *27*, 108981.
65. Ball, G., Aljabar, P., Arichi, T., Tsur, N., Cox, D., Merchant, N., Nongena, P., Hajnal, J.V., Edwards, A.D., and Counsell, S.J. (2016). Machine-learning to characterise neonatal functional connectivity in the preterm brain. *Neuroimage* *124*, 267–275.
66. Alcauter, S., Lin, W., Smith, J.K., Short, S.J., Goldman, B.D., Reznick, J.S., Gilmore, J.H., and Gao, W. (2014). Development of thalamocortical connectivity during infancy and its cognitive correlations. *J. Neurosci.* *34*, 9067–9075.
67. Eyre, M., Fitzgibbon, S.P., Ciarrusta, J., Cordero-Grande, L., Price, A.N., Poppe, T., Schuh, A., Hughes, E., O’Keeffe, C., Brandon, J., et al. (2021). The Developing Human Connectome Project: typical and disrupted perinatal functional connectivity. *Brain* *144*, 2199–2213. <https://doi.org/10.1093/brain/awab118>.
68. Bhutta, A.T., Cleves, M.A., Casey, P.H., Craddock, M.M., and Anand, K.J.S. (2002). Cognitive and behavioral outcomes of school-aged children who were born preterm: a meta-analysis. *JAMA* *288*, 728–737.
69. Saigal, S., and Doyle, L.W. (2008). An overview of mortality and sequelae of preterm birth from infancy to adulthood. *Lancet* *371*, 261–269.
70. Di Biase, M.A., Tian, Y.E., Bethlehem, R.A.I., Seidlitz, J., Alexander-Bloch, A.F., Yeo, B.T.T., and Zalesky, A. (2023). Mapping human brain charts

- cross-sectionally and longitudinally. *Proc. Natl. Acad. Sci.* *120*, e2216798120. <https://doi.org/10.1073/pnas.2216798120>.
71. Chen, L., Wu, Z., Hu, D., Wang, Y., Zhao, F., Zhong, T., Lin, W., Wang, L., and Li, G. (2022). A 4D infant brain volumetric atlas based on the UNC/UMN baby connectome project (BCP) cohort. *Neuroimage* *253*, 119097. <https://doi.org/10.1016/j.neuroimage.2022.119097>.
 72. Cox, R.W. (1996). AFNI: software for analysis and visualization of functional magnetic resonance neuroimages. *Comput. Biomed. Res.* *29*, 162–173.
 73. Jenkinson, M., Beckmann, C.F., Behrens, T.E.J., Woolrich, M.W., and Smith, S.M. (2012). *Fsl. Neuroimage* *62*, 782–790.
 74. Avants, B.B., Epstein, C.L., Grossman, M., and Gee, J.C. (2008). Symmetric diffeomorphic image registration with cross-correlation: Evaluating automated labeling of elderly and neurodegenerative brain. *Med. Image Anal.* *12*, 26–41. <https://doi.org/10.1016/j.media.2007.06.004>.
 75. Shi, F., Wang, L., Dai, Y., Gilmore, J. H., Lin, W., and Shen, D. (2012). LABEL: pediatric brain extraction using learning-based meta-algorithm. *NeuroImage* *62*, 1975–1986.
 76. Du, H., Xia, M., Zhao, K., Liao, X., Yang, H., Wang, Y., and He, Y. (2018). PAGANI Toolkit: Parallel graph-theoretical analysis package for brain network big data. *Human brain mapping* *39*, 1869–1885.
 77. Wang, Y., Du, H., Xia, M., Ren, L., Xu, M., Xie, T., Gong, G., Xu, N., Yang, H., and He, Y. (2013). A Hybrid CPU-GPU Accelerated Framework for Fast Mapping of High-Resolution Human Brain Connectome. *PLoS One* *8*, e62789. <https://doi.org/10.1371/journal.pone.0062789>.
 78. Eden, E., Navon, R., Steinfeld, I., Lipson, D., and Yakhini, Z. (2009). GOrilla: a tool for discovery and visualization of enriched GO terms in ranked gene lists. *BMC Bioinf.* *10*, 48. <https://doi.org/10.1186/1471-2105-10-48>.
 79. Subramanian, A., Tamayo, P., Mootha, V.K., Mukherjee, S., Ebert, B.L., Gillette, M.A., Paulovich, A., Pomeroy, S.L., Golub, T.R., Lander, E.S., and Mesirov, J.P. (2005). Gene set enrichment analysis: A knowledge-based approach for interpreting genome-wide expression profiles. *Proc. Natl. Acad. Sci.* *102*, 15545–15550. <https://doi.org/10.1073/pnas.0506580102>.
 80. Mootha, V.K., Lindgren, C.M., Eriksson, K.-F., Subramanian, A., Sihag, S., Lehar, J., Puigserver, P., Carlsson, E., Ridderstråle, M., Laurila, E., et al. (2003). PGC-1 α -responsive genes involved in oxidative phosphorylation are coordinately downregulated in human diabetes. *Nat. Genet.* *34*, 267–273. <https://doi.org/10.1038/ng1180>.
 81. Bayley, N. (2006). *Bayley Scales of Infant and Toddler Development*.
 82. Power, J.D., Barnes, K.A., Snyder, A.Z., Schlaggar, B.L., and Petersen, S.E. (2012). Spurious but systematic correlations in functional connectivity MRI networks arise from subject motion. *Neuroimage* *59*, 2142–2154. <https://doi.org/10.1016/j.neuroimage.2011.10.018>.
 83. Hughes, E.J., Winchman, T., Padormo, F., Teixeira, R., Wurie, J., Sharma, M., Fox, M., Hutter, J., Cordero-Grande, L., Price, A.N., et al. (2017). A dedicated neonatal brain imaging system. *Magn. Reson. Med.* *78*, 794–804.
 84. Eklund, A., Nichols, T.E., and Knutsson, H. (2016). Cluster failure: Why fMRI inferences for spatial extent have inflated false-positive rates. *Proc. Natl. Acad. Sci.* *113*, 7900–7905. <https://doi.org/10.1073/pnas.1602413113>.
 85. Charrad, M., Ghazzali, N., Boiteau, V., and Niknafs, A. (2014). NbClust: an R package for determining the relevant number of clusters in a data set. *J. Stat. Softw.* *61*, 1–36.
 86. Wood, S.N. (2017). *Generalized Additive Models: An Introduction with R*, Second Edition (CRC Press).

STAR★METHODS

KEY RESOURCES TABLE

REAGENT or RESOURCE	SOURCE	IDENTIFIER
Deposited data		
Neuroimaging data from dHCP	Developing Human Connectome Project	https://biomedica.github.io/dHCP-release-notes/download.html
Neuroimaging data from BCP	Baby Connectome Project	https://nda.nih.gov/edit_collection.html?id=2848
Developmental gene expression dataset	BrainSpan Atlas	http://www.brainspan.org/
UNC_4D_Volume_template	Chen et al. ⁷¹	https://www.nitrc.org/projects/uncbcp_4d_atlas/
Code and data used	This paper	https://zenodo.org/records/10932391
Software and algorithms		
AFNI	Cox ⁷²	https://afni.nimh.nih.gov/
FSL	Jenkinson et al. ⁷³	https://fsl.fmrib.ox.ac.uk/fsl/fslwiki
SPM12	N/A	https://www.fil.ion.ucl.ac.uk/spm/
ANTs	Avants et al. ⁷⁴	https://ants.gouv.fr/
skullStripping toolkit	Shi et al. ⁷⁵	https://www.nitrc.org/projects/skulltoolkit
PAGANI toolbox	Du et al. ⁷⁶ ; Wang et al. ⁷⁷	https://www.nitrc.org/projects/pagani_toolkit/
SeeCAT	N/A	https://www.nitrc.org/projects/seecat/
BrainNet Viewer	Xia et al. ³⁷	http://www.nitrc.org/projects/bnv/
MATLAB	N/A	N/A
Rstudio	N/A	https://www.rstudio.com/
Louvain algorithm	Blondel et al. ³⁹	N/A
Generalized additive mixed model (GAMM)	N/A	N/A
Support vector regression (SVR)	N/A	N/A
Gorilla tool	Eden et al. ⁷⁸	http://cbl-gorilla.cs.technion.ac.il/
REVIGO	N/A	http://revigo.irb.hr/
Gene set enrichment analysis (GSEA)	Subramanian et al. ⁷⁹ ; Mootha et al. ⁸⁰	https://www.gsea-msigdb.org/gsea/index.jsp

RESOURCE AVAILABILITY

Lead contact

Further information and requests for resources and data should be directed to and will be fulfilled by the lead contact, Yong He (yong.he@bnu.edu.cn).

Materials availability

This study did not generate new unique reagents.

Data and code availability

- The dHCP and BCP datasets are publicly available. Accession numbers are listed in the [key resources table](#).
- All original code has been deposited at Zendo and is publicly available as of the date of publication. DOIs are listed in the [key resources table](#).
- Any additional information required to reanalyze the data reported in this paper is available from the [lead contact](#) upon request.

EXPERIMENTAL MODEL AND STUDY PARTICIPANT DETAILS

Participants

This study used two publicly available longitudinal imaging datasets, the dHCP and the BCP, focusing on the perinatal and postnatal periods.

The BCP dataset was rigorously screened to ensure that participants met specific health criteria. Details of these criteria are discussed in detail in ref.³³. Briefly, the BCP dataset excludes any child born before 37 weeks of gestation, with a birth weight

of less than 2000 g, or who suffered significant delivery complications such as neonatal hypoxia or required a prolonged stay in the NICU (more than two days). Other exclusion criteria were as follows: 1) adoption; 2) having a first-degree relative diagnosed with autism, intellectual disability, schizophrenia, or bipolar disorder; 3) presence of significant medical or genetic conditions influencing growth, development, or cognition; 4) contraindications for undergoing MRI scans; and 5) maternal pre-eclampsia, placental abruption, positive maternal HIV status, maternal use of alcohol or illicit drugs during pregnancy, and the inability of caregivers to consent in English.

The inclusion criteria for the dHCP dataset focused primarily on: 1) pregnant women with fetal age estimated from the last menstrual period and confirmed, if possible, by an early ultrasound scan at 20–42 weeks' gestation; and 2) live infants aged between 23 and 44 weeks gestational age, estimated from the mother's last menstrual period and confirmed, if possible, by an early ultrasound scan. Exclusion factors for the dHCP dataset included: 1) mothers or infants with any contraindications to MRI, such as the presence of metallic implants (e.g., orthopedic devices or non-MRI-compatible clips for patent ductus arteriosus closure); 2) preterm infants deemed too fragile to undergo the duration of the scan, despite fully supportive neonatal care, as determined by the attending pediatric doctor in consultation with the infant's medical team; and 3) language barriers that could impede proper communication about the study or the consent process.

Neurocognitive assessments

Neonates from the dHCP were assessed with the Bayley Scales of Infant and Toddler Development, Third Edition (BSID-III) at around 1.5 years of age, adjusted for prematurity (19.3 ± 2.22 months). The BSID-III includes five distinct scales designed to comprehensively assess different domains of development, including cognitive, language, and motor scales for the infants. Specifically, the cognitive scale of the BSID-III focuses on assessing sensorimotor development, concept formation, memory, basic problem-solving, and reasoning skills.⁸¹ Meanwhile, the language scale includes two subscales that assess receptive and expressive communication, gauging the child's capacity to understand spoken language, follow instructions, and use language effectively to identify or describe objects and people. The motor scale assesses both gross and motor skills, such as visual tracking, reaching for objects, maintaining balance, and the capability to perform actions such as jumping.⁸¹ The neurocognitive assessments were carried out by a certified neurodevelopmental psychologist.

MRI quality control procedure

BCP structural MRI quality control

Initially, we downloaded the BCP dataset (https://nda.nih.gov/edit_collection.html?id=2848), comprising 343 infants with 812 scans. Subsequently, we conducted a comprehensive quality control and data cleaning process for the structural images, encompassing the following steps (Figure S1A).

1. Scan Dates and Ages Verification for Longitudinal Data:

i) Identified 9 infants with two scans at both month 0 and 1, where the two scans within each pair were identical. We removed the scans labeled as 1 month, assuming they were intended to represent 0 months based on the file name. ii) Found 16 scans with incorrectly labeled ages. Detailed information is provided in Table S1. Due to uncertainty about the correct ages, 6 scans were discarded.

2. Structural MRI Verification:

Eliminated 9 scans without released structural images, as these scans lacked either T1-weighted (T1w) or T2-weighted (T2w) images.

3. "qc_outcome" Label Verification:

We employed the "qc_outcome" label that was provided in the released document as an initial quality control. If recorded as failure, the scan was eliminated, resulting in a total elimination of 7 scans.

4. Radiological Review:

Three experienced neuroradiologists specializing in pediatric MRI visually examined each scan. Infants with abnormal structures of potential clinical or analysis significance, such as cysts, cerebellum abnormalities, and perivascular spaces, were excluded. Consequently, 51 scans were excluded.

5. Head Motion Score Assessment:

Two experienced researchers assessed the head motion for each scan using a four-level scale (3-none, 2-mild, 1-moderate, and 0-severe). The four examples of the four-level scale can be found in Figure S1B. Scans with a head motion score below 2 were excluded, leading to the exclusion of 41 scans.

6. Signal Interference Check:

Identified a situation where signals from the baby's hand interfered with signals from the brain. Consequently, 2 scans were excluded.

In conclusion, the final BCP structural images comprised 296 infants with 687 scans after rigorous quality control and data cleaning.

BCP task-free functional MRI quality control

There were 292 infants with 587 task-free functional MRI scans released. The data quality control process involved several key steps.

1. Volume Consistency Check:

For the BCP dataset, the standard volume count for an fMRI scan is 420. Scans that had incomplete volumes were identified and excluded, resulting in the removal of 8 scans.

2. Structural MRI Verification:

Each functional MRI scan was cross-checked to ensure the existence of a corresponding structural MRI. A total of 60 scans which lacked structural images were eliminated.

3. Head Motion Evaluation:

We evaluated head motion through the mean frame-wise displacement and the proportion of volumes with frame-wise displacement greater than 0.5 mm. The frame-wise displacement was calculated as the sum of the absolute values of the derivatives of the six translational and rotational parameters.⁸² The mean frame-wise displacement (mFD) was computed as head motion parameter for each fMRI scan. The threshold for significant head motion was defined as an mFD greater than 0.5 and more than 40% of volumes being outliers. This criterion aimed to balance data retention with quality control. Based on these parameters, 42 scans were found ineligible due to excessive head motion.

4. Preprocessed Scans Inspection:

A thorough visual inspection was conducted on all preprocessed, task-free functional MRI scans. Those showing issues with registration or other preprocessing steps were excluded from further analysis. After careful inspection, 19 scans were excluded.

Consequently, the final BCP dataset comprised 458 task-free fMRI scans from 222 infants.

dHCP dataset quality control

We downloaded the dHCP dataset release 3³² from (<https://biomedica.github.io/dHCP-release-notes/download.html>), comprising of 887 scans from 783 neonates. The data quality control process involved several key steps.

1. Radiology Score Exclusion:

Scans from neonates with high radiology scores (>2), indicative of structural or signal irregularities with potential clinical significance or significance for analysis, were excluded. This decision was made by a specialist perinatal neuroradiologist, culminating in the exclusion of 218 scans.

2. "qc_fmri_comment" Evaluation:

We analyzed the "qc_fmri_comment" column available in the released document (https://github.com/BioMedIA/dHCP-release-notes/blob/master/supplementary_files/combined.tsv). Scans without reportable fMRI QC issues or with remarks irrelevant to our study's objectives (e.g., missing surface data; failed fMRI recon) were kept. This criterion led to the exclusion of 81 scans.

3. Head Motion Evaluation:

We excluded fMRI scans showing significant head motion, defined by a mean frame displacement greater than 0.5 mm or when over 40% of the volumes exhibited frame displacement. This threshold aligns with the standards utilized in the BCP dataset, resulting in 93 scans being excluded.

4. Preprocessed Scans Inspection:

Scans exhibiting registration or other preprocessing issues were excluded, affecting 23 scans.

In total, the two combined datasets included 665 infants with 930 fMRI scans. Specifically, the dHCP dataset included 443 infants (202 females) aged 28–45 post-menstrual weeks. The BCP dataset included 222 infants (119 females) aged 0–3 years. The distribution of participant age and longitudinal visits is shown in [Figures S2A](#) and [S2B](#), respectively.

METHOD DETAILS

Image acquisition

MRI images from the dHCP dataset were acquired on a 3T Philips Achieva scanner at St. Thomas Hospital, London. A neonate-dedicated head coil consisting of 32 channel was used.⁸³ T2-weighted images were obtained using a Turbo Spin Echo (TSE) sagittal sequence with the following parameters: TR/TE = 12000/156ms, SENSE factor 2.11 (axial) and 2.60 (sagittal). For task-free fMRI, a multiband (MB) 9 × accelerated echo-planar imaging technique was employed for 15min, with following parameters: TE/TR = 38/392ms, 2300 volumes, and an acquired spatial resolution of 2.15 mm isotropic. Additionally, single-band reference scans were also acquired, utilizing bandwidth-matched readout, along with spin echo acquisitions in both anterior-posterior/posterior-anterior (AP/PA) phase encoding directions.

MRI images from the BCP dataset were collected using a 3T Siemens Prisma MRI scanner equipped with a Siemens 32 channel head coil at the University of North Carolina at Chapel Hill and University of Minnesota.³³ T1-weighted images (208 sagittal slices) were acquired through a 3D magnetization-prepared rapid gradient echo (3D-MPRAGE) sequence with the following parameters: TR/TE/TI = 2400/2.24/1600ms, flip angle = 8, acquisition matrix = 320 × 320, and resolution = 0.8 mm isotropic. T2-weighted images (208 sagittal slices) were acquired using turbo spin-echo sequences (turbo factor = 314, echo train length = 1166ms) with the following parameters: TR/TE = 3200/564ms, flip angle = VAR, and resolution = 0.8 mm isotropic. The fMRI scans were acquired using a blood oxygenation level-dependent (BOLD) contrast-sensitive gradient echo echo-planar sequence with the following parameters: TR/TE = 800/37ms, flip angle = 80, field of view (FOV) = 208 × 208 mm, 72 axial slices per volume, resolution = 2 mm isotropic, total volumes = 420. Single-band reference scans and AP/PA scans with opposite phase encoding directions were also acquired.

MRI preprocessing

The BOLD fMRI images were preprocessed using Analysis of Functional NeuroImages (AFNI, Version AFNI_17.0.08)⁷² and FMRIB Software Library (FSL 6.0.1).⁷³ For the BCP dataset, we conducted the following steps: (i) removal of the first 10 volumes; (ii) reorientation for consistency across dataset; (iii) head motion correction. The fMRI volumes linearly registered to its corresponding single-band EPI reference image (SBRef) when available. In the absence of an SBRef, the initial volume was used for linear registration, followed by registration to the mean of these initially registered fMRI volumes. Head motion parameters did not significantly correlate with scan age (mFD: $r = -0.04$, $p = 0.28$). (iv) distortion correction; Geometric distortions were corrected using the posterior-anterior/anterior-posterior flipped scan pairs. (v) normalization. Specifically, images were first linearly aligned to their corresponding high-resolution T1/T2-weighted images (T1w: older than 6 months, T2w: younger than 6 months). Subsequently, they underwent nonlinearly registration to age-specific templates⁷¹ using ANTs SyN diffeomorphic registration,⁷⁴ and then linear registration to the common 6-month template. By pairwise registration between all age-specific templates, the target template with the least deformation was selected as the common template. The Jacobin determinant of the pairwise deformation was shown in [Figure S3A](#). The aligned functional data were normalized using the transformation estimated from the two registration steps mentioned above, maintaining 2 mm isotropic voxels. (vi) spatial smoothing with a Gaussian kernel (full width at half-maximum of 4 mm). (vii) linear trend removal; (viii) nuisance regression; Nuisance regressors, including the Friston's 24 motion parameters, white matter signal, cerebrospinal fluid signal, and global signal, as well as the scrubbing parameters (volumes with displacement greater than 0.5 mm from the previous volume), were regressed out of the time series. (ix) temporal band-pass filtering (0.01–0.1 Hz). For the dHCP dataset, we used the downloaded distortion and motion corrected 4D images (func/sub-{subid}_ses-{sesid}_task-rest_desc-mcddc_bold.nii.gz) for preprocessing. The steps from normalization (v) to temporal band-pass filtering (ix) were applied, using the same protocol as described for the BCP dataset.

Functional connectivity matrix construction

In this study, we constructed the functional correlation matrices at a voxel level considering no proper parcellation during this specific age range. The gray matter mask (53499 voxels in total) was predefined by applying a threshold to the gray matter probability template of 6 months. Pearson's correlation was calculated between the BOLD time series of every pair of voxels within the gray matter mask. To enhance the normal distribution of correlation coefficients, Fisher's z transformation was utilized, and the positive values of all correlations were used to determine the correlation for each participant. Notably, any connectivity that terminated within 10 mm of the center of each voxel was assigned zero to prevent potential shared signals between neighboring voxels.

Functional connectivity strength analysis

To explore age effects on functional connectivity, we computed voxel-wise functional connectivity strength (FCS) values for an overall description. Specifically, the FCS for each voxel was obtained by averaging the correlations between that voxel and all other voxels in the brain. To examine developmental effects on nodal FCS, we conducted a voxel-wise analysis using a generalized additive mixed model (GAMM). This model has flexibility to investigate both linear and nonlinear relationships between variables and age (see [developmental effects analysis](#)). We set the significance threshold for nodal FCS at $p < 0.001$ at the voxel level with Gaussian random field (GRF) correction at the cluster level of $p < 0.05$.⁸⁴ The fitted FCS values were mapped onto the brain surface to visualize developmental changes. To illustrate the diverse patterns of developmental trajectories, we categorized all regions with significant FCS development into four distinct clusters. This categorization was done based on the similarity of developmental trajectories of FCS

within each cluster. To determine the most suitable number of clusters, we relied on indices from the NbClust packages.⁸⁵ According to the distribution of optimal cluster number (Figure S3B), we categorized the regions with significant FCS development into four distinct patterns and showed their developmental trajectories of mean FCS values. To further investigate whether the local or global functional connectivity predominately influences the FCS development, we investigated the age effects of functional connectivity using the GAMM. The functional connectivity was computed as the Pearson's correlation between the average time series of voxels within each cluster and the time series from all voxels.

Hubs were identified as regions with high FCS values ($>$ mean +1.5 std) and were outlined on the fitted age-specific FCS maps. To explore the distribution of hubs across different functional systems, we mapped the Yeo's atlas³⁶ on the 6-month infant brain. First, we nonlinearly registered the MNI152 template to the BCP 24-month template using ANTs SyN algorithm. Then, we linearly registered it to the 6-month template. The combined deformation was applied to Yeo's 7 network atlas in MNI152 space. We computed the voxel number of hubs in each functional system at different ages and presented them in the bar plot. We also computed the hub voxel ratio as the voxel number in each functional system to the total hub voxel number. The age-related changes of the hub voxel ratio in each functional system were fitted with GAMM respectively.

To further explore the distance effects on age-related connectivity changes, FCS was calculated at different distance bins. This involved calculating the Euclidean distance, D_{ij} , as an approximate anatomical distance of functional connectivity between voxel i and voxel j , and dividing the whole brain's functional connectivity maps into three bins, 10–30 mm, 30–50 mm, and $>$ 50 mm. For each voxel, we calculated FCS for each distance bin. We then performed voxel-wise GAMM analysis to explore the age effects on distance-dependent FCS, while correcting for multiple comparisons within the corresponding gray matter mask due to varying voxel numbers in different distance bins. To further investigate the developmental trajectory of FCS across different distance bins, we performed a principal component analysis (PCA) on all individual's FCS within each distance bin. This approach considered the entire brain's developmental trajectory rather than focusing on a single voxel property. Using GAMM, we fitted the loading coefficient trajectory of the first principal component, which reflected the global trajectory of FCS across all voxels. We computed the first-order difference value of the loading coefficient trajectory to evaluate the developmental rate of FCS changes in different distance bins. Furthermore, we identified the peak age of FCS (first-order difference value = 0).

Graph theory measures analysis

Functional brain networks were constructed by applying a 5% density threshold to the correlation matrices and binarizing them. These analyses of voxel-wise brain networks were executed using our Parallel Graph-theoretical Analysis (PAGANI) toolbox (https://www.nitrc.org/projects/pagani_toolkit/).^{76,77} Graph theoretical metrics, including the clustering coefficient and nodal efficiency, were employed to assess functional segregation and integration. Specifically, the clustering coefficient is the fraction of triangles around a node and quantifies the extent to which a node's neighbors in the graph are interconnected. The nodal efficiency measures how efficiently a node communicates with other nodes, calculated as the average shortest path length of the node in the network. The GAMM model was utilized to investigate the age effect on the mean clustering coefficient and the mean nodal efficiency at both global and voxel levels. For the nodal analysis, we set the significance threshold at $p < 0.001$ at the voxel level, with Gaussian random field (GRF) correction at the cluster level of $p < 0.05$. To further examine the changes in functional segregation and integration across the cortex, we performed data-driven PCA on the clustering coefficient and nodal efficiency at the voxel-level respectively, as shown in Figure 2B. The aim of this PCA was to identify the spatial axis that account for the greatest variance in how the measure changed with age. This approach considered the entire developmental trajectory of the measure, rather than focusing on a single age-related property. The first principal component generated by this PCA comprised voxel loadings that captured variations in maturational profiles across a low-dimensional embedding. To visually depict the developmental trajectories of the measures along the spatial axis, we divided the axis into 10 decile bins and calculated the average measures across all voxels within each bin. Subsequently, the GAMM model was employed to fit the average measure changes with age.

Module analysis

To deepen our understanding of the developmental patterns of functional connectomes at the system level, we investigated the modular organization of brain networks. To conduct modular analysis, we applied the Louvain algorithm implemented in the PAGANI Toolkit, known for its speed and accuracy in detecting communities within large networks,³⁹ to individual brain networks. The algorithm works by identifying modules that maximize the modularity measure Q value through a two-stage iterative process. Modularity measures the extent to which a network can be divided into densely connected modules or communities that have sparse connections to other modules. The process begins with maximizing local modularity by reallocating each node to the community where it contributes the most to increasing modularity. Next, a network of hypernodes representing the previously identified communities is formed, setting the stage for another round of optimization. The completion of the algorithmic process provides two key outputs: the modularity, Q , which offers a numerical representation of the modular partitioning of the network, and a vector detailing the community membership for each node. These results form the basis for the subsequent calculation of the participant coefficient, which provides insights into the modular structure of the network and the role of the nodes within it. The participation coefficient measures the diversity of a node's connections across modules. Additionally, we calculated the within-module functional connectivity and between-module functional connectivity to quantify functional segregation and integration. The within-module functional connectivity represents the average connectivity between any two voxels within the same module, while the between-module

functional connectivity represents the average connectivity between any two voxels in different modules. To explore the age effects on within-/between-module functional connectivity and the nodal participation coefficient, we employed the GAMM. For the nodal participation coefficient, we set the significance threshold at $p < 0.001$ at the voxel level, with Gaussian random field (GRF) correction at the cluster level of $p < 0.05$. Furthermore, we mapped the fitted participation coefficient at various ages onto the surface to observe developmental changes. To capture the spatial axis of participation coefficient changes across voxels, we performed the same PCA process to the nodal participation coefficient measure as mentioned above. We divided the loadings into 10 decile bins based on the loadings of the first PC and calculated the average participation coefficient for all voxels within each bin. Finally, we used the GAMM to fit the average measures' changes with age.

To investigate the functional module assignment changes across ages, we utilized a sliding window approach for module detection in group functional networks, as shown in Figure 3D. The functional connectivity matrices were divided into age windows, progressing from the youngest to the oldest. The age window was centered from 28 weeks to 184 weeks (3 years old) with a step of 2 weeks. The initial age window ranged from 28 weeks to 29 weeks, and the final window stretched from 183 weeks to 184 weeks. This process yielded 113 overlapping sub-grouped functional brain networks. Within each window, we computed the average functional connectivity matrices to obtain the group functional brain networks, and subsequently conducted module detection in each group functional network using the Louvain algorithm. To address the lack of correspondence in module division across different time windows, we adjusted the module labels to align them as closely as possible. The window with the highest number of modules was chosen as the reference window, and the module index in other windows was reassigned according to the extent of overlap with the module in the reference window. This method only modified the module labels without changing the module partition. The module assignment across various ages was then visualized using a Sankey plot, as shown in Figure 3E. Additionally, we calculated the flexibility of module assignment across age windows. Nodal flexibility represents the number of times of a node changes its community assignment across age windows, normalized by the total number of possible changes (total number of age windows - 1).

Prediction analysis of neurocognitive outcomes

Given the critical role of early brain development in shaping later cognitive growth, our study aimed to explore how connectome-based neuroimaging measures predict later neurocognitive outcomes. The BCP dataset has a continuous age distribution, whereas the dHCP dataset has collected neuroimaging data at birth and neurocognitive data at subsequent follow-up. Taking this into account, we used the neuroimaging data from full-term dHCP neonates to predict their neurocognitive scores recorded at 1.5 years of age. The cohort consisted of 321 neonates with paired neuroimaging and neurocognitive data, including assessments of cognitive, language and motor skills. Neuroimaging predictors included global mean FCS, mean clustering coefficient, mean nodal efficiency, modularity and within-module FC, all of which showed significant age-related changes. To predict the individual neurocognitive scores, we used the support vector regression (SVR) model with a linear kernel function regressing out covariates such as scan age, the interval between birth and scan, age at neurocognitive assessment, sex and mFD. We evaluated the performance of the regression model using 10-fold cross-validation, where the dataset was divided into ten parts, ensuring that each segment served as the validation set once over ten cycles, while the remaining data formed the training set. To determine the accuracy of our predictions for each neurocognitive outcome, we compared the actual scores and the predicted scores using Pearson correlation. In particular, we conducted a permutation test 10,000 times with randomly shuffled neurocognitive scores to determine whether the predictive performance exceeded chance levels. Analyses were also performed at the voxel level including FCS, clustering coefficient, and nodal efficiency.

Gene expression analysis

To explore the underlying molecular mechanisms of functional connectome development, we utilized the developmental gene expression dataset, BrainSpan Atlas,^{34,35} to study the gene expression differences between brain regions that exhibited significant and non-significant age-related changes in FCS. The BrainSpan Atlas encompasses transcriptomic data—including 52376 genes—from 524 brain samples taken from 42 individuals ranging in age from eight post-conceptual weeks to 40 postnatal years. This dataset covers 11 neocortical areas and 5 additional regions. The brain regions included in our investigation are listed in Table S4 (excluding the cerebellar cortex). We focused on the transcriptomic data of genes obtained from donors aged between 28 post-menstrual weeks and 3 years. This included a total of 105 samples from 9 donors. We categorized 61 samples as 'significant (sig)' and 44 samples as 'non-significant (non-sig)' according to Table S4. To ensure robust results, genes contributed by fewer than six donors at different ages were excluded, leaving a subset of 26874 genes derived from the 105 samples.

The expression level for each gene was z-scored across all samples. We tested the difference in expression level for each gene between significant ("sig" samples) and non-significant ("non-sig" samples) regions using the one-sided Wilcoxon rank-sum test. Multiple comparisons were corrected using the false discovery rate (FDR), with a q-value of less than 0.05.⁴¹ Genes with significant expression differences were subjected to Gene Ontology (GO) enrichment analysis using the Gorilla tool (<http://cbl-gorilla.cs.technion.ac.il/>).⁷⁸ The genes with significant expression differences were used as the target gene list and all 26874 genes were as the background list. All three ontology categories, including biological process, molecular function, and cellular component, were examined. Specifically, GO terms with p -value less than 10^{-5} and FDR less than 0.05 are reported in the main results. We summarized the long lists of GO terms and removed redundant GO terms using the online tool REVIGO (<http://revigo.irb.hr/>).

Gene set enrichment analysis (GSEA)^{79,80} was then used to assess whether genes associated with typical neurodevelopmental processes and neuronal metabolic pathways were overrepresented at the extremes (top or bottom) of the gene list ranked by the effect size of expression differences between 'sig' and 'non-sig' samples. Specifically, we evaluated eight gene sets based on previous works covering typical neurodevelopmental processes²² including dendrite development (103 genes), synapse development (104 genes), neuron differentiation (103 genes), neuron migration (101 genes), axon development (101 genes) and myelination (105 genes), as well as major neuronal metabolic pathways including aerobic glycolysis (116 genes)²⁸ and oxidative phosphorylation (82 genes).⁴⁰ For each gene set, we obtained an enrichment score (ES) representing the degree of enrichment. The ES was calculated by going through the ranked gene list, increasing a running-sum statistic when encountering a gene in the previous gene set and decreasing it when encountering genes not in the previous gene set. The statistical significance of the ES was estimated using permutation tests by shuffling the phenotype labels 10,000 times. To account for differences in gene set size, we compared the enrichment score with those estimated by permutation tests and derived a normalized enrichment score (NES). The NES was calculated as the actual ES divided by the mean ESs against all permutations of the dataset. Enrichment analysis was performed using the clusterProfiler package (<https://bioconductor.org/packages/release/bioc/html/clusterProfiler.html>) and visualized using the gseaplot2 function in the enrichplot package (<https://bioconductor.org/packages/release/bioc/html/enrichplot.html>).

QUANTIFICATION AND STATISTICAL ANALYSIS

Developmental effects analysis

To investigate the developmental effects, we fitted a generalized additive mixed model (GAMM), which is flexible to examine both linear and nonlinear relationships between variables and age. This model included age as a smooth term, with subject ID as a random effect, and sex, mFD, and site as linear covariates to control for potential confounding factors. We used the cubic splines as the basis set for the smooth term, which provide computational efficiency and are suitable when data are sparse at the boundaries, and the restricted maximum likelihood (REML) approach for the selection of smoothing parameters, which allows unbiased estimation of variance components in random effects models.⁸⁶ The smoothing term for age produces a spline, modeled by weighted basis functions, that represents the developmental trajectory for each metric. To select the appropriate basis function complexity (k), we compared the Bayesian information criterion (BIC) values of global variable fitting models when $k = 3$ and $k = 4$ (Table S4). It was found that the majority of variables had lower BIC values at $k = 3$ compared to $k = 4$, and it was evident that for other variables, the BIC values showed little difference between $k = 3$ and $k = 4$. Consequently, we chose $k = 3$ to limit the flexibility of the smooth term, although the exact value of k needs to be informed by model diagnostics to optimally balance fit and parsimony for all variables. All ages are in weeks.

When examining sex differences, we aimed to determine whether the effect of age varied by sex. To do this, we specified two GAMMs: one including an interaction term between age and sex, and the other excluding this interaction. Both models included the subject ID as a random effect, with sex, mFD, and site as linear covariates. We then performed an analysis of variance (ANOVA) to compare the two models. The purpose of this comparison was to assess whether the inclusion of the interaction term significantly improved the fit of the model.

To evaluate the effectiveness of the GAMM in mitigating site effects, we conducted a residual-based analysis. After fitting the GAMM model, we extracted the residuals, which represent the differences between the observed values and the values predicted by the model. We then performed an ANOVA with the residuals as the independent variable and the site as a factor to test whether there was a significant difference in the mean residuals between the two sites. Ideally, if site effects are adequately controlled, the residuals should not be significantly different between the two sites. As can be seen in Figure S5, the residuals obtained from the models fitted for these metrics showed no significant differences between the two sites, indicating that the models have effectively controlled for site-specific effects.